Continuum Mech. Thermodyn. (2019) 31:851–884
https://doi.org/10.1007/s00161-018-0689-8

ORIGINAL ARTICLE

Francesco dell'Isola · Pierre Seppecher · Jean Jacques Alibert · Tomasz Lekszycki · Roman Grygoruk · Marek Pawlikowski · David Steigmann · Ivan Giorgio · Ugo Andreaus · Emilio Turco · Maciej Gołaszewski · Nicola Rizzi · Claude Boutin · Victor A. Eremeyev · Anil Misra · Luca Placidi · Emilio Barchiesi · Leopoldo Greco · Massimo Cuomo · Antonio Cazzani · Alessandro Della Corte · Antonio Battista · Daria Scerrato · Inna Zurba Eremeeva · Yosra Rahali · Jean-François Ganghoffer · Wolfgang Müller · Gregor Ganzosch · Mario Spagnuolo · Aron Pfaff · Katarzyna Barcz · Klaus Hoschke · Jan Neggers · François Hild

Pantographic metamaterials: an example of mathematically driven design and of its technological challenges

Received: 9 March 2018 / Accepted: 21 May 2018 / Published online: 30 June 2018

Abstract In this paper, we account for the research efforts that have been started, for some among us, already since 2003, and aimed to the design of a class of exotic architectured, optimized (meta) materials. At the first stage of these efforts, as it often happens, the research was based on the results of mathematical investigations. The problem to be solved was stated as follows: determine the material (micro)structure governed by those equations that specify a desired behavior. Addressing this problem has led to the synthesis of second gradient materials. In the second stage, it has been necessary to develop numerical integration schemes and

Communicated by Andreas Öchsner.

F. dell'Isola · U. Andreaus · E. Barchiesi (✉)
Dipartimento di Ingegneria Strutturale e Geotecnica, Università degli Studi di Roma "La Sapienza.", Via Eudossiana 18, 00184 Rome, Italy
E-mail: barchiesiemilio@gmail.com

F. dell'Isola · P. Seppecher · T. Lekszycki · I. Giorgio · E. Turco · V. A. Eremeyev · A. Misra · L. Placidi · E. Barchiesi · L. Greco · M. Cuomo · A. D. Corte · A. Battista · D. Scerrato · I. Z. Eremeeva · J.-F. Ganghoffer
International Research Center M&MoCS, Università degli Studi dell'Aquila, Via Giovanni Gronchi 18 - Zona industriale di Pile, 67100 L'Aquila, Italy

F. dell'Isola · A. D. Corte
Dipartimento di Ingegneria Civile, Edile-Architettura e Ambientale, Università degli Studi dell'Aquila, Via Giovanni Gronchi 18 - Zona industriale di Pile, 67100 L'Aquila, Italy

F. dell'Isola · I. Giorgio · L. Placidi · E. Barchiesi · A. D. Corte · A. Battista · D. Scerrato · M. Spagnuolo
Research Institute for Mechanics, National Research Lobachevsky State University of Nizhni Novgorod, Nizhny Novgorod, Russia

P. Seppecher · J. J. Alibert
Institut de Mathématiques de Toulon, Université de Toulon et du Var, Avenue de l' Université, BP 132, 83957 La Garde Cedex, France

T. Lekszycki · R. Grygoruk · M. Pawlikowski · M. Gołaszewski · K. Barcz
Institute of Mechanics and Printing, Warsaw University of Technology, 85 Narbutta Street, 02-524 Warsaw, Poland

T. Lekszycki
Department of Experimental Physiology and Pathophysiology, Medical University of Warsaw, 1b Banacha Street, 02-097 Warsaw, Poland

the corresponding codes for solving, in physically relevant cases, the chosen equations. Finally, it has been necessary to physically construct the theoretically synthesized microstructures. This has been possible by means of the recent developments in rapid prototyping technologies, which allow for the fabrication of some complex (micro)structures considered, up to now, to be simply some mathematical dreams. We show here a panorama of the results of our efforts (1) in designing pantographic metamaterials, (2) in exploiting the modern

D. Steigmann
Department of Mechanical Engineering, University of California at Berkeley, 6133 Etcheverry Hall, Mailstop 1740, Berkeley, CA, USA

E. Turco
Dipartimento di Architettura, Design, Urbanistica, Università degli Studi di Sassari, Asilo Sella, Via Garibaldi 35 (I piano), 07041 Alghero, SS, Italy

N. Rizzi
Dipartimento di Architettura, Università degli studi Roma Tre, Via della Madonna dei Monti 40, 00184 Rome, Italy

C. Boutin
Ecole Nationale des Travaux Publics de l'Etat, LGCB CNRS 5513 - CeLyA, Université de Lyon, 69518 Vaulx-en-Velin Cedex, France

V. A. Eremeyev
Faculty of Civil and Environmental Engineering, Gdańsk University of Technology, ul. Gabriela Narutowicza 11/12, 80-233 Gdańsk, Poland

V. A. Eremeyev
Mathematics, Mechanics and Computer Science Department, South Federal University, Milchakova, str., 8a, Rostov-on-Don, Russia 344090

A. Misra
Civil, Environmental and Architectural Engineering Department, The University of Kansas, 1530 W. 15th Street, Lawrence, KS 66045-7609, USA

L. Placidi
Engineering Faculty, International Telematic University Uninettuno, C.so Vittorio Emanuele II 39, 00186 Rome, Italy

L. Greco · M. Cuomo
Dipartimento di Ingegneria Civile ed Ambientale (sezione di Ingegneria Strutturale), Università di Catania, Edificio Polifunzionale, IV piano, Viale Andrea Doria, 6 I, 95125 Catania, Italy

A. Cazzani
Dipartimento di Ingegneria Civile, Ambientale e Architettura, Università degli studi di Cagliari, Via Marengo 2, Cagliari, Italy

A. Battista
Laboratoire des Sciences de l'Ingénieur pour l' Environnement, Université de La Rochelle, 23 avenue Albert Einstein, BP 33060, 17031 La Rochelle, Italy

Y. Rahali · J.-F. Ganghoffer
Laboratoire d'Energétique et de Mécanique Théorique et Appliquée, University of Lorraine, 2 Avenue de la Foret de Haye, BP 90161, 54505 Vandoeuvre-lés-Nancy cedex, France

W. Müller · G. Ganzosch
Faculty of Mechanics, Berlin University of Technology, Einsteinufer 5, 10587 Berlin, Germany

M. Spagnuolo
Laboratoire des Sciences des Procédés et des Matériaux, Université Paris 13, Campus de Villetaneuse 99 avenue Jean-baptiste Clément, 93430 Villetaneuse, France

A. Pfaff · K. Hoschke
Fraunhofer Institute for High-Speed Dynamics, Ernst-Mach-Institut, Eckerstraße 4, 79104 Freiburg, Germany

technology of rapid prototyping, and (3) in the mechanical testing of many real prototypes. Among the key findings that have been obtained, there are the following ones: pantographic metamaterials (1) undergo very large deformations while remaining in the elastic regime, (2) are very tough in resisting to damage phenomena, (3) exhibit robust macroscopic mechanical behavior with respect to minor changes in their microstructure and micromechanical properties, (4) have superior strength to weight ratio, (5) have predictable damage behavior, and (6) possess physical properties that are critically dictated by their geometry at the microlevel.

Keywords Pantographic fabrics · Metamaterials · Scientific design · Higher gradient materials

Introduction

Like every other human activity, the design, manufacturing and testing of prototypes of novel materials having a complex and purpose-tailored (micro)structure need the organized efforts of many specialists having a large scope of competence. Therefore, the present work needed the collaboration of many scientists, each one with his/her own specific competences. The order of the authors of this paper has been formed with a simple criterion: it is related to the length of the time period that has seen their involvement in the described joint research efforts and, therefore, does not express any evaluation of the importance of each contribution.

Let us note that, in this paper, no specific length scale is attached to the word "micro." Specifically, with its use it is meant that at one or at multiple smaller (with respect to the unique macroscale corresponding to that at which phenomena are observed) length scales the material is made of complex microstructures: they consist in the organization of the distribution of matter and its (possibly varying) physical properties.

The aim of this paper is to account, in a unique panoramic view, for the research efforts that we have started (at least the first ones among us) since 2003 and that has produced, in our opinion, some interesting results. The aim of the investigations was more specifically (1) to design novel and exotic architectured metamaterials based on a mathematical understanding of the related mechanical problems and on suitably designed numerical simulations, (2) to build the designed prototypes by using 3D printing technology, (3) to test with sensitive apparatuses the so-built prototypes, (4) to elaborate the obtained data with modern image correlation techniques, (5) to produce a careful model fitting of the experimental data by means of the systematic use of numerical simulations, and (6) to compare the proposed models with experimental evidence.

At the first stage of the research effort, as it often happens, the problem was approached from a theoretical point of view. The mathematical models, which were initially introduced, belong to the class of generalized continua: the introduced independent kinematic fields include not only the displacement field but, eventually, also microstretch and/or microrotation fields. The particular class of second gradient continua was more specifically considered: in these media, the strain energy depends on the displacement gradient and on its second gradient. The reasons of their name are therefore clear: in second gradient continua the strain energy may depend on the second gradient of displacement. Second gradient continua can be regarded as media endowed with a tensorial microstructure in which a constraint is applied, namely it requires that the microstructure tensor is equal to the placement gradient. The problem to be solved was: given a desired behavior, to find at first the evolution equations modeling such a behavior and then to characterize the material (micro)structure governed by the chosen equations.

In the second stage, it was necessary to develop numerical integration schemes and the corresponding codes for solving, in physically relevant cases, the equations chosen to describe the desired behavior. Finally, it was necessary to build the microstructures. This was possible by means of the recent developments of rapid prototyping technologies, which allow for the fabrication of those which, up to now, were simply mathematical dreams.

In this paper, we show the results of our efforts in designing pantographic metamaterials, in the mechanical testing of real prototypes, and evidence is provided on their exotic behavior. With the latest advancements (e.g., 3D-printing technology and, more generally, of rapid prototyping techniques), the small-scale production of materials with complex geometries has become more affordable than ever [1–4]. The exploitation of these new technologies has made possible the development in the last few years of materials with very different substructures.

J. Neggers · F. Hild
Laboratoire de Mécanique et Technologie (LMT), ENS Paris-Saclay/CNRS/Université Paris-Saclay, 61 avenue du Président Wilson, 94235 Cachan Cedex, France

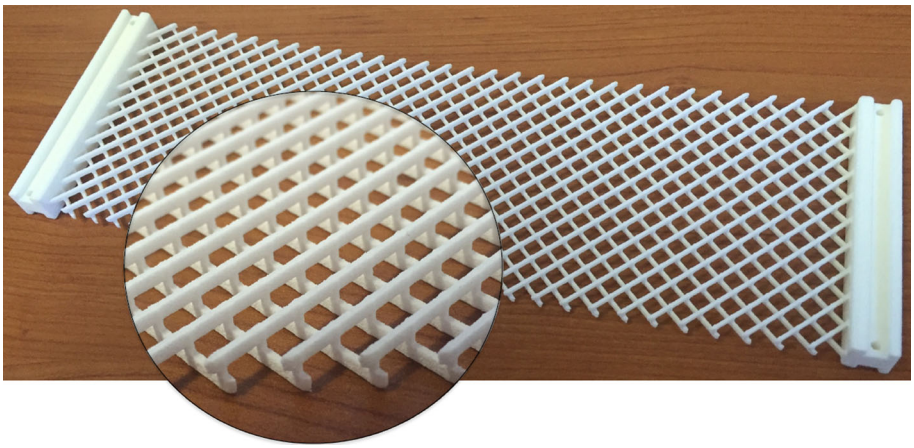

Fig. 1 Example of pantographic structure [13]

One of the research goals whose achievement has been sped up by rapid prototyping is to determine and study new microstructures that, at a well-specified macroscopic scale, exhibit a behavior that can be described by nonstandard mathematical models like generalized continuum theories. Many of these theories, that today are being called "generalized" (as opposed to "classical" theories), were formulated before or together with so-called "classical" theories and then lost [5,6]. It is possible to state that some of these theories were already known at least two centuries ago [7,8]. Pantographic structures (Fig. 1) have been proposed as a metamaterial [9], which is well described by second gradient continuum theories [10–12].

1 Modeling and experiments in elastic regime

The theoretical interest in pantographic structures derives from the fact that, in order to describe their exotic phenomenology, one has to utilize higher gradient continuum theories [14,15] or micromophic theories [16,17] with the related problem of homogenization [18] and of different strategies for numerical integration [19,20].

1.1 Homogenization of periodic truss modular structures

Throughout the history of mechanics, several multiscale procedures have been developed in order to relate macromodels with micromodels, the first attempts tracing back to Maxwell and Saint-Venant [21]. An approach that has proven to be effective is based on the postulate of a macroscopic and a microscopic model and of a kinematic correspondence between the deformations defined within the two models. Successively, it is postulated that the power expended in corresponding motions coincides. In this way, it is possible to obtain the coefficients of the constitutive equations of the macromodel in terms of properties of the building blocks constituting the microscopic model. The macromodel is not the result of the homogenization process but is, instead, assumed a priori. Formal asymptotic expansion can help to encompass this difficulty, and a microscopic model made up of linear Euler beams leads to a simple macroscopic second gradient model of a 1D planar beam [11].

The structure that is considered at the microlevel is the so-called pantographic structure (Fig. 2). It is assumed that the considered pantographic microstructure is made up of a very large number of small modules and the limit behavior when such a number tends to infinity, i.e., the homogenized macromodel, is studied. Using Gamma-convergence technique, it is proven that the homogenized model is the postulated second gradient model [11]. Successively, a modified (Warren-type) pantographic structure is proposed as micromodel in order to get for the first time a third gradient planar beam model (Fig. 3), whose general properties were already studied by Mindlin and Tiersten [22], and Dillon and Perzyna [23]. Such structures possess other floppy modes (i.e., placements for which the strain energy vanishes) than, trivially, rigid motions. The pantographic beam does not store any energy when undergoing uniform extension, while the Warren-type pantographic beam does not store any energy when undergoing uniform flexure.

In Ref. [24], formal asymptotic expansion procedures, already employed [11,13], are systematically considered in the framework of linear elasticity in order to determine the effective behavior of periodic structures

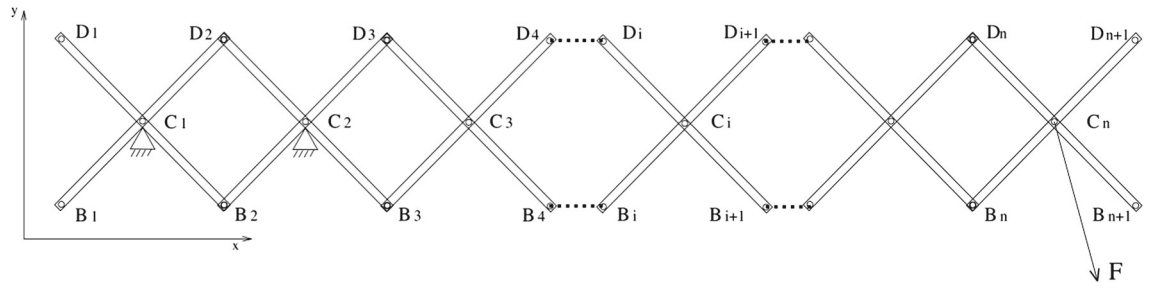

Fig. 2 Pantographic microstructure considered in Ref. [11]

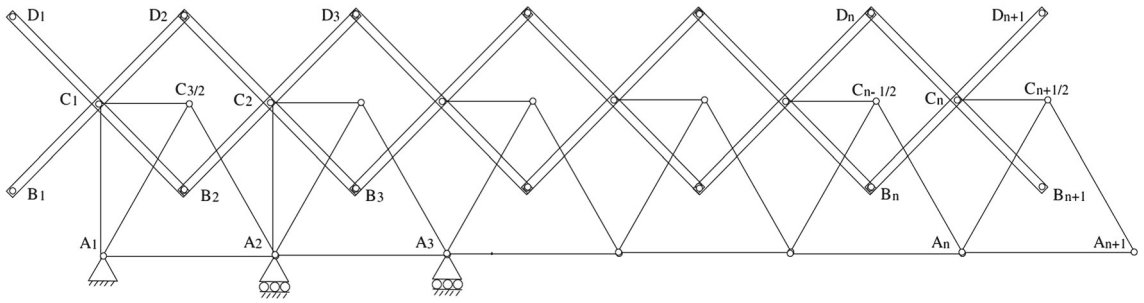

Fig. 3 Warren-type pantographic microstructure [11]

made of welded elastic bars. Noting that flexural and torsional stiffnesses of isotropic homogeneous elastic bars are much smaller than the extensional one entails an asymptotic rescaling of stiffnesses giving rise to interesting macromodels. In Ref. [24], different examples of two-dimensional or three-dimensional microstructures that lead to generalized 1D, 2D or 3D continua like Timoshenko beam, Mindlin-Reissner plate, strain gradient, Cosserat, or micromorphic continua are provided.

Reference [25], in the spirit of pantographic fabrics, addresses one of the main challenges in the modern theory of materials: the determination of those microstructures that produce, at the macrolevel, a class of metamaterials whose elastic range is many orders of magnitude wider than the one exhibited by "conventional" materials. With pantographic microstructures, which are made of "long" microbeams, it is possible to obtain metamaterials whose elastic range spans up to an elongation exceeding 30%. It is shown that the same behavior can be obtained by means of an internal microstructure based on a king post pattern (Fig. 4). This solution shows many advantages, namely it only involves microbeams; all beams are only undergoing extension or contraction; all internal constraints are terminal pivots. While the elastic strain energy can be determined as easily as in the case of a long-beam microstructure, the proposed design seems to have remarkable advantages: it seems to be more damage resistant and, therefore, to be able to have a wider elastic range; it can be obtained with the same three-dimensional printing technology; it seems to be less subject to compression buckling. The following analyses were carried out: (1) the derivation of Hencky-type discrete models for king post trusses, (2) the application of an effective integration scheme to a class of relevant deformation tests for the proposed metamaterial, and (3) the numerical determination of an equivalent second gradient continuum model.

1.2 Pipkin elastic plate model with inextensible fibers

Starting from a number of papers by Pipkin et al. [26–33], 2D continua consisting of two orthogonal families of inextensible fibers were considered [34] and an adaptation to the case of pantographic structures has been presented [10,35]. First, a $2D$ continuum, whose reference shape is given by the rectangular domain $\Omega \subset \mathbb{R}^2$ with the tallest side three times longer than the shorter one, has been considered. Considering only planar motions, the current shape of Ω is described by the suitably regular macro-placement $\boldsymbol{\chi} : \Omega \to \mathbb{R}^2$, with $(X_1, X_2) \overset{\boldsymbol{\chi}}{\mapsto} (x_1, x_2)$. An orthogonal frame of reference $(\mathcal{O}, \xi_1, \xi_2)$, whose orientation is the same of the inextensible fibers in the reference configuration and whose coordinates are dimensionless, is introduced. Accordingly, we have

$$\xi_1 := \frac{1}{l}(X_1 - X_2) + \frac{1}{2} \quad , \quad \xi_2 := \frac{1}{l}(X_1 + X_2) + \frac{1}{2}. \tag{1}$$

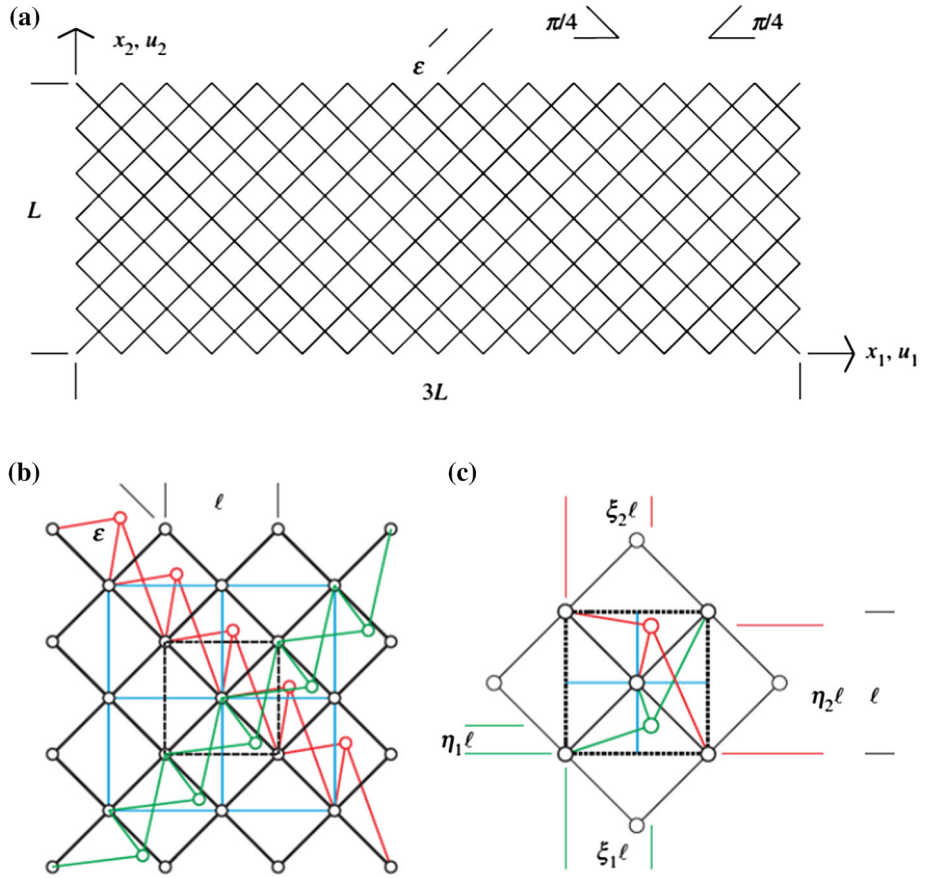

Fig. 4 King post pantographic lattice: geometry (**a**), pantographic rods (in black), king post rods (in red and green), auxiliary rods (in cyan) (**b**), and king post geometric parameters (**c**) (color figure online)

A graphical depiction of the introduced quantities is given in Fig. 5. A pair (D_1, D_2) of orthonormal vectors, the basis associated with the frame of reference $(\mathcal{O}, \xi_1, \xi_2)$, is further introduced. The two vectors D_1 and D_2 are tangent to the two families of fibers in the reference configuration. The inextensibility constraint can be encoded in the following way. A curve β is inextensible for a placement $\boldsymbol{\chi}$ if, for every part α of β, $\boldsymbol{\chi}(\alpha)$ has the same length of α.

By definition d_1 and d_2 are considered to be the push-forward vectors, in the current configuration, of the vectors D_1 and D_2, respectively, i.e., $d_\alpha = FD_\alpha$, $\alpha = 1, 2$, where $F = \nabla\boldsymbol{\chi}$. The inextensibility constraint implies that $\|d_1(\xi_1, \xi_2)\| = \|d_2(\xi_1, \xi_2)\| = 1$ for all (ξ_1, ξ_2) such that $\boldsymbol{\chi}$ is locally continuously differentiable. In the celebrated Rivlin paper [36], it is stated that when $\boldsymbol{\chi}$ is twice continuously differentiable on an open simply linearly connected subset Δ of Ω, the fiber inextensibility assumption allows the following representation formula

$$\boldsymbol{\chi}^{\Delta}(\xi_1, \xi_2) = \boldsymbol{\chi}_1^{\Delta}(\xi_1) + \boldsymbol{\chi}_2^{\Delta}(\xi_2) \tag{2}$$

to be found for the restriction to Δ of the placement. If $\mu_1^{\Delta}(\xi_1)$ and $\nu_1^{\Delta}(\xi_1)$ denote the projections of $\boldsymbol{\chi}_1^{\Delta}(\xi_1)$ on D_1 and D_2, respectively, and $\nu_2^{\Delta}(\xi_2)$ and $\mu_2^{\Delta}(\xi_2)$ the projections of $\boldsymbol{\chi}_2^{\Delta}(\xi_1)$ on D_1 and D_2, respectively, then

$$\boldsymbol{\chi}_1^{\Delta}(\xi_1) = \mu_1^{\Delta}(\xi_1)D_1 + \nu_1^{\Delta}(\xi_1)D_2 \quad \text{and} \quad \boldsymbol{\chi}_2^{\Delta}(\xi_2) = \nu_2^{\Delta}(\xi_2)D_1 + \mu_2^{\Delta}(\xi_2)D_2 \tag{3}$$

The map $\boldsymbol{\chi}$ is assumed to be piecewise twice continuously differentiable. It is worth noting that the matrix representation of F on the subset Δ and for the reference frame defined by D_1 and D_2 is expressed as

$$[F^{\Delta}]_{(D_1,D_2)} = \begin{bmatrix} \mu_{1,1}^{\Delta}(\xi_1) & \nu_{2,2}^{\Delta}(\xi_2) \\ \nu_{1,1}^{\Delta}(\xi_1) & \mu_{2,2}^{\Delta}(\xi_2) \end{bmatrix} \tag{4}$$

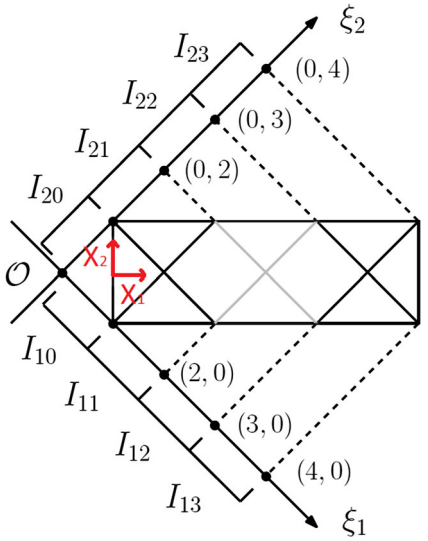

Fig. 5 Material (Lagrangian) coordinates adapted to inextensible fiber configuration [10]

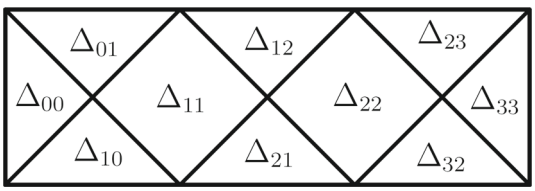

Fig. 6 Domain pattern induced by the boundary conditions [10]

and that the functions $\boldsymbol{\chi}_\alpha^\Delta(\xi_\alpha)$ ($\alpha = 1, 2$) are determined up to two scalar constants C_1 and C_2, i.e., if the decomposition (2) holds with the representation (3), then the following alternative representation holds

$$\begin{aligned}\boldsymbol{\chi}_1^\Delta(\xi_1) &= \left(\mu_1^\Delta(\xi_1) + C_1\right) D_1 + \left(\nu_1^\Delta(\xi_1) + C_2\right) D_2\\ \boldsymbol{\chi}_2^\Delta(\xi_2) &= \left(\nu_2^\Delta(\xi_2) - C_1\right) D_1 + \left(\mu_2^\Delta(\xi_2) - C_2\right) D_2\end{aligned} \tag{5}$$

The inextensibility constraint, together with the assumption that the map $\boldsymbol{\chi}$ be piecewise C^2, implies that there exist two quantities $\vartheta_1^\Delta(\xi_1)$ and $\vartheta_2^\Delta(\xi_2)$ such that

$$d_1^\Delta = \cos\vartheta_1(\xi_1) D_1 + \sin\vartheta_1(\xi_1) D_2 \ \text{ and } \ d_2^\Delta = \sin\vartheta_2(\xi_2) D_1 + \cos\vartheta_2(\xi_2) D_2 \tag{6}$$

The above statement stands since d_1^Δ and d_2^Δ belong to $S_2 = \{x \in \mathbb{R}^2 : \ \|x\| = 1\}$.

Let Σ_1 and Σ_2 denote the left and right short sides, respectively, of the boundary $\partial\Omega$ of Ω. The following boundary conditions are considered:

1. vanishing displacement on Σ_1;
2. nonvanishing displacement u_0 on Σ_2.

Because of fiber inextensibility, the boundary conditions on Σ_1 and Σ_2 determine the placement field not just at the boundary, but also in some regions of the interior of Ω [34] , i.e., on the regions Δ_{00} and Δ_{33} of Fig. 6.

Hence, the space of admissible placements for the Pipkin continuum under study is uniquely determined by the continuous piecewise twice continuously differentiable fields $\mu_1(\xi_1)$ and $\mu_2(\xi_2)$. In particular, given the boundary conditions i.e., $\mu(\xi)$ is known on Δ_{00} and Δ_{33} (for $\xi_\alpha \in [0, 1] \cup [3, 4]$), we are interested in determining $\mu_\alpha(\xi_\alpha)$ only for $\xi_\alpha \in [1, 3]$. By looking at the ordinary differential equations

$$\frac{\mathrm{d}\mu_\alpha(\xi_\alpha)}{\mathrm{d}\xi_\alpha} = \cos\vartheta_\alpha(\xi), \quad \alpha = 1, 2 \tag{7}$$

which derive from Eqs. (5) and (6). Providing an integration constant through the continuity condition $\mu_\alpha(1) = 1$ at point $(1, 1)$ uniquely defines the space of admissible placements for the Pipkin continuum by means of the fields $\vartheta_1(\xi_1)$ and $\vartheta_2(\xi_2)$.

In fiber-inextensible 2D Pipkin continua, it is customary to introduce the *shear deformation* γ as a strain measure. The shear deformation is defined as the scalar product of the fiber directions in the deformed configuration and, reminding the inextensibility assumption and Eq. (6), reads

$$\gamma(\xi_1, \xi_2) := d_1 \cdot d_2 = \cos\left(\frac{\pi}{2} - \vartheta_1(\xi_1) - \vartheta_2(\xi_2)\right) = \sin\left(\vartheta_1(\xi_1) + \vartheta_2(\xi_2)\right) \tag{8}$$

The following kinematic constraint should be enforced

$$-\frac{\pi}{2} < \vartheta_1 + \vartheta_2 < \frac{\pi}{2} \ (\Longrightarrow \ -1 < \gamma < 1) \tag{9}$$

if the case $\vartheta_1 + \vartheta_2 = \pm\frac{\pi}{2}$, which stands for overlapping fibers is to be avoided. Now that the space of fields $\vartheta_1(\xi_1)$ and $\vartheta_2(\xi_2)$ uniquely describes admissible placements, the strain energy density $W(\vartheta_1, \vartheta_2, \frac{\mathrm{d}\vartheta_1}{\xi_1}, \frac{\mathrm{d}\vartheta_2}{\xi_2})$ is introduced. It is assumed to have the form

$$W\left(\vartheta_1, \vartheta_2, \frac{\mathrm{d}\vartheta_1}{\xi_1}, \frac{\mathrm{d}\vartheta_2}{\xi_2}\right) = \alpha g(f(\gamma)) + \beta g(\|\nabla f(\gamma)\|) \tag{10}$$

with $g(x) = \frac{1}{2}x^2$. Different functions f have been studied [10,35], among which:

S $f(\gamma) = \gamma$
Q $f(\gamma) = \arcsin\gamma$
T $f(\gamma) = \tan(\arcsin\gamma)$

Henceforth the case $\alpha = 1$, $\beta = 0$ is referred to as *first gradient* (1g), and $\alpha = 0$, $\beta = 1$ as *second gradient* (2g). Numerical results [37–41] show that the final configurations obtained by using second gradient energies are smoother than those with the first gradient approach. In the following, numerical results will be reported for standard bias extension, shear and rotation tests, which confirm such a statement. Among all experiment, the bias test has been extensively analyzed. In a standard bias extension test, $u_{01} = u_{02} := u_0$. Then, a new property has to be enforced on the placement function $\boldsymbol{\chi}$, which holds true for the bias extension test, while not, e.g., for the shear tests that will be considered later on. Only placements functions that are symmetric with respect to the X_1 axis can be considered. With regard to the reference frame $(\mathcal{O}, \xi_1, \xi_2)$, this means that given a point P of coordinates (ξ, η) and its symmetric (with respect to X_1) P_S whose coordinates are (η, ξ), the conditions

$$d_1(P) \cdot D_\alpha = d_2(P_S) \cdot D_{3-\alpha} \ \alpha = 1, 2 \tag{11}$$

must be satisfied. They imply that $\nu_{1,1}(\xi) = \nu_{2,2}(\xi)$ and $\mu_{1,1}(\xi) = \mu_{2,2}(\xi)$ and in turn, given the boundary conditions, $\nu_1(\xi) = \nu_2(\xi) := \nu(\xi)$ and $\mu_1(\xi) = \mu_2(\xi) := \mu(\xi)$. It is thus possible to state that in a standard bias test the space of admissible placements for the Pipkin continuum is uniquely determined by the (globally continuous) piecewise twice continuously differentiable field $\mu(\xi)$. Since $\mu(\xi)$ is known on Δ_{00} and Δ_{33}, i.e., for $\xi \in [0, 1] \cup [3, 4]$, we are interested in determining $\mu(\xi)$ only for $\xi \in [1, 3]$. By analyzing ordinary differential equations

$$\frac{\mathrm{d}\mu_\alpha(\xi)}{\mathrm{d}\xi} = \cos\vartheta_\alpha(\xi), \ \alpha = 1, 2 \tag{12}$$

it is concluded that $\vartheta_1(\xi) = \vartheta_2(\xi) := \vartheta(\xi)$ with $\vartheta(\xi)$ a (possibly discontinuous) piecewise continuously differentiable field. Numerical results are shown in Figs. 7 and 8. Figure 7 provides a general overview of the qualitative differences among different choices of α, β and of the function f in Eq. (10). In Fig. 8, a comparison between final shapes of the rectangular sample is reported when modeled with $1gT$ and $2gT$ strain energy densities. It is noteworthy that the final shapes are much smoother when a second gradient model is employed, as strong variations of the field variable are penalized in the energy.

Let us now turn to reporting shear tests. Thus, the symmetry assumptions, which were previously introduced when dealing with the standard bias extension test, are no longer considered. When modeling the shear test, the condition $u_{01} = -u_{02}$ holds. The results are shown in Figs. 9 and 10. In particular, Fig. 9 gives an overview of the qualitative differences among different choices of α, β and of the function f defined in Eq. (10). The non-monotonicity of the $1gS$ and $2gS$ models is not physically grounded. Besides, in Fig. 10 comparisons between final shapes of the rectangular samples, modeled with $1gT$ and $2gT$ strain energy density, are reported. Again, the final shapes are much smoother when a second gradient model is employed.

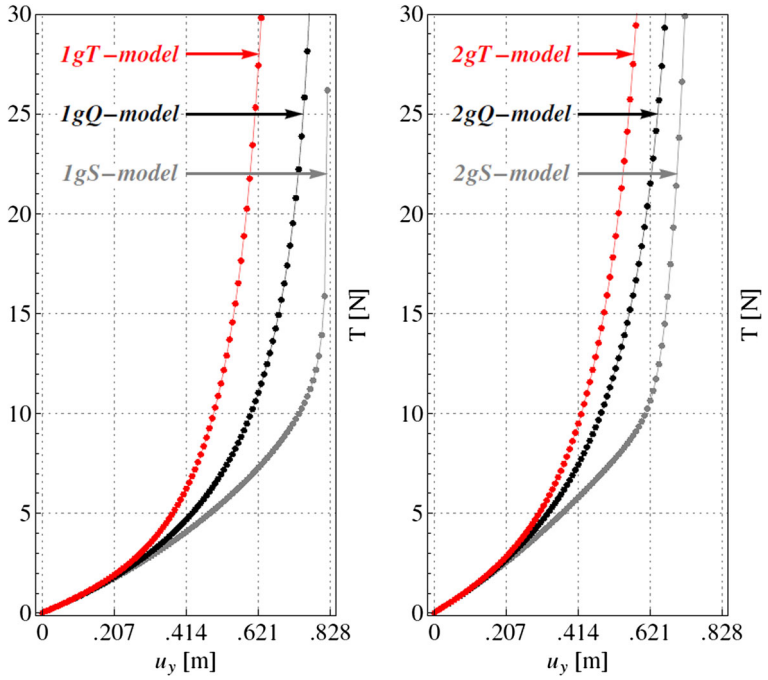

Fig. 7 Bias extension test. Resultant (normal) forces on the short side (computed by means of Castigliano's first theorem) versus vertical component of prescribed displacement: **a** first gradient energy models, **b** second gradient energy models

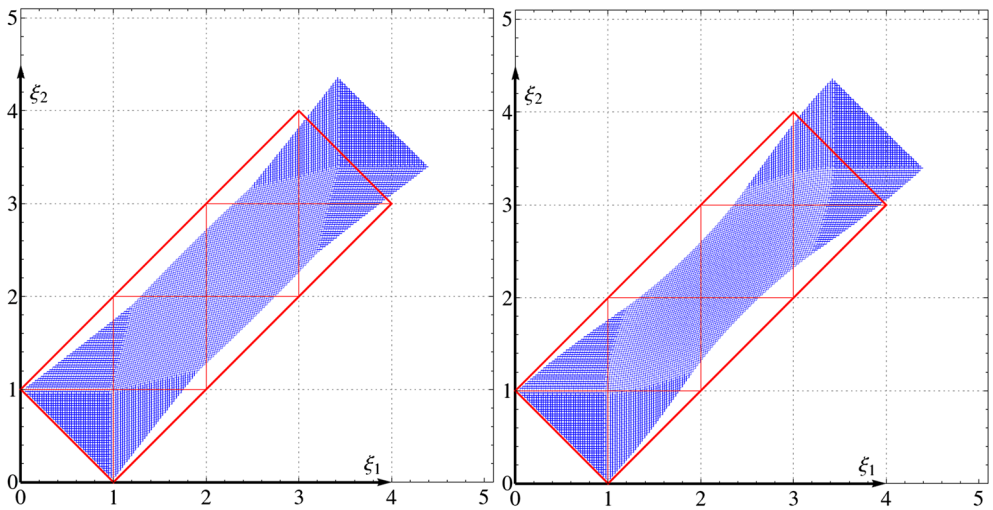

Fig. 8 Bias extension test. Reference and deformed configurations for the first gradient $1gT$ (left) and second gradient $2gT$ (right) models

1.3 Discrete Hencky-type elastic plate model

A discrete approach has been introduced for pantographic structures [13] and subsequently studied [42,43]. Modeling assumptions for the micromodel are based on physically grounded considerations about the real microstructure of pantographic sheets and apply to the case of large deformations. In particular, trying to comply with reported experimental evidences [10,13], the extension of fibers is accounted for by connecting adjacent material particles with extensional springs. Moreover, at each node of the lattice, rotational springs, which are deformed when the angle spanned by two contiguous extensional springs is changed, are introduced. To account for the fact that such materials show two privileged material directions, a Lagrangian Cartesian orthonormal coordinate system is introduced. Its associated basis of unit vectors is (D_1, D_2) made of two

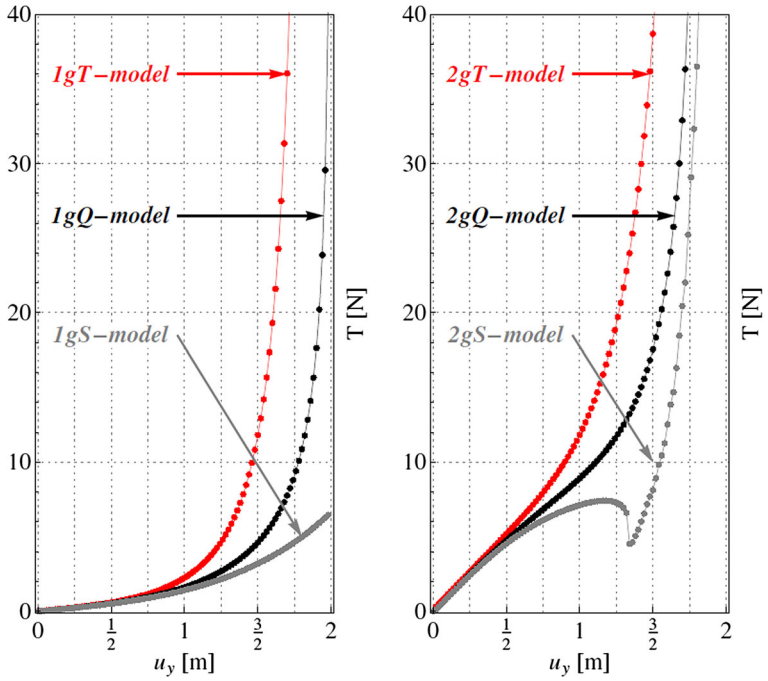

Fig. 9 Shear test. Resultant (shear) forces on the short side (computed by means of Castigliano's first theorem) versus vertical component of prescribed displacement: **a** first gradient energy models, **b** second gradient energy models

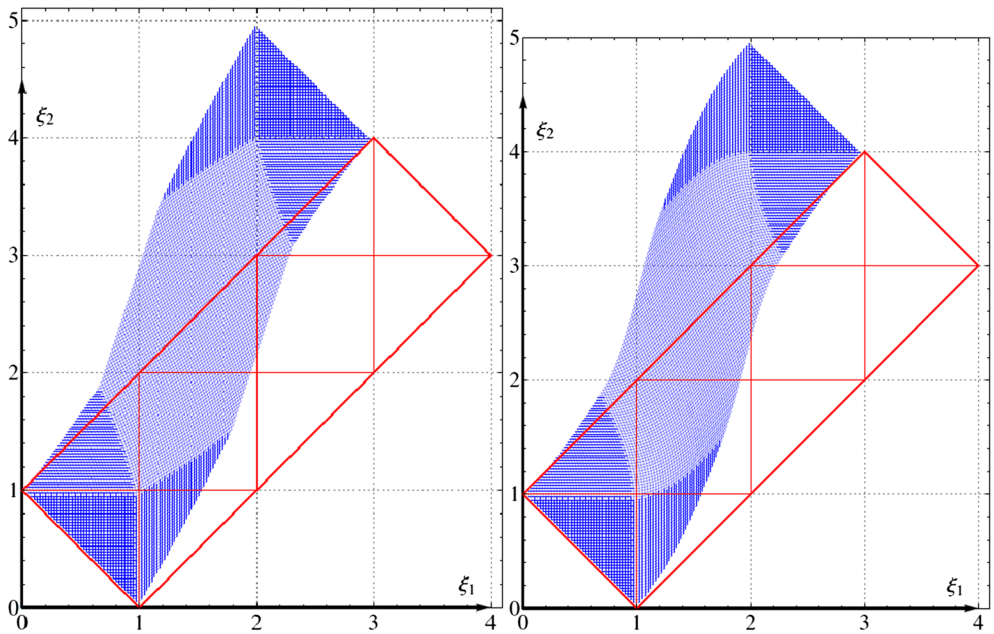

Fig. 10 Shear test. Reference and deformed configurations for the first gradient $1gT$ (left) and second gradient $2gT$ (right) models

orthonormal vectors that represent the directions of the families of fibers constituting the pantographic structure in the reference configuration. In such configuration, the lattice body points are located at the positions

$$P_{i,j} = (i\epsilon, j\epsilon), \quad i = 0, 1, \ldots, N \text{ and } j = 0, 1, \ldots, M \tag{13}$$

and $p_{i,j}$ denotes the current configuration position of the body point placed at $P_{i,j}$ in the reference configuration. The body points at the nodes $P_{i,j}$ are connected by extensional springs along each one of the coordinate lines

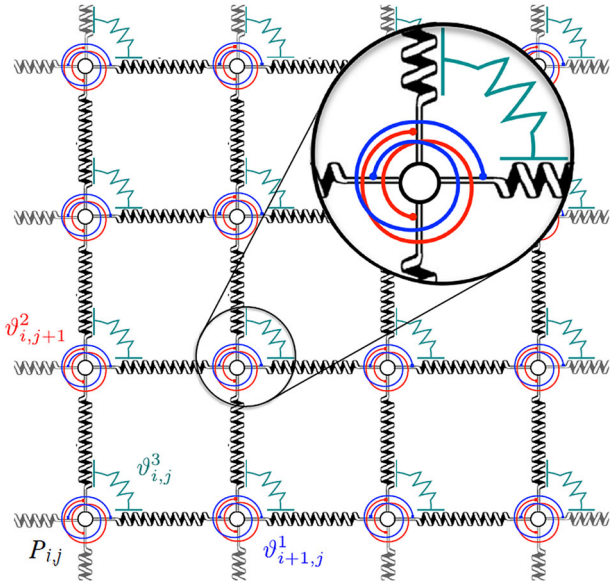

Fig. 11 Micromodel of a pantographic sheet with a detail of the three rotational springs [13]

(Fig. 11) and their deformation energies depend on the distances between adjacent contiguous points in the current configuration, i.e., on the distance between $p_{i,j}$ and $p_{i,j+1}$ for the fibers parallel to D_1 in the reference configuration, and on the distance between $p_{i,j}$ and $p_{i+1,j}$ for the fibers parallel to D_2 in the reference configuration. The first type of extensional spring is characterized by the rigidity $k^1_{i,j}$ and the second kind by $k^2_{i,j}$. Such extensional rigidities are related to the extensional behavior, respectively, of the two families of fibers. As mentioned before, at each node there are also three rotational springs whose deformation energies depend, respectively, on the angles:

1. $\vartheta^1_{i,j}$ formed by the vectors $p_{i-1,j} - p_{i,j}$ and $p_{i+1,j} - p_{i,j}$,
2. $\vartheta^2_{i,j}$ formed by the vectors $p_{i,j-1} - p_{i,j}$ and $p_{i,j+1} - p_{i,j}$,
3. $\vartheta^3_{i,j}$ formed by the vectors $p_{i,j+1} - p_{i,j}$ and $p_{i+1,j} - p_{i,j}$.

The postulated strain energy for the microscopic Lagrangian discrete system having its configuration specified by the set of parameters $\{p_{i,j}\}$ reads

$$\begin{aligned} U(\{p_{i,j}\}) = &\sum_j \sum_i \frac{k^1_{i,j}}{2}(\|p_{i+1,j} - p_{i,j}\| - \epsilon)^2 + \sum_j \sum_i b^1_{i,j}(\cos\vartheta^1_{i,j} + 1) \\ &+ \sum_j \sum_i \frac{k^2_{i,j}}{2}(\|p_{i,j+1} - p_{i,j}\| - \epsilon)^2 + \sum_j \sum_i b^2_{i,j}(\cos\vartheta^2_{i,j} + 1) \\ &+ \sum_j \sum_i \frac{b^3_{i,j}}{2}\left|\vartheta^3_{i,j} - \frac{\pi}{2}\right|^{\xi} \end{aligned} \tag{14}$$

On the one hand, the rigidities $b^1_{i,j}$ and $b^2_{i,j}$ are related, respectively, to the bending behavior of the two families of fibers. The rigidities $b^3_{i,j}$, on the other hand, are associated with the torsional stiffness of the pivots connecting the two families of fibers, ξ being a parameter that is equal to 2 for a standard linear case.

In subsequent papers [42,43], the discrete (elastic) quasi-static Hencky-type spring model, made of extensional and rotational (i.e., torsional) springs, is solved at each iteration by energy minimization. Even if the model does not contemplate external forces, it would be very easy to consider the discrete analogous forces leading, after a homogenization like the one presented later on, to external bulk forces and double forces. In Fig. 12, the equilibrium shape resulting from a standard bias extension test simulation using the strain

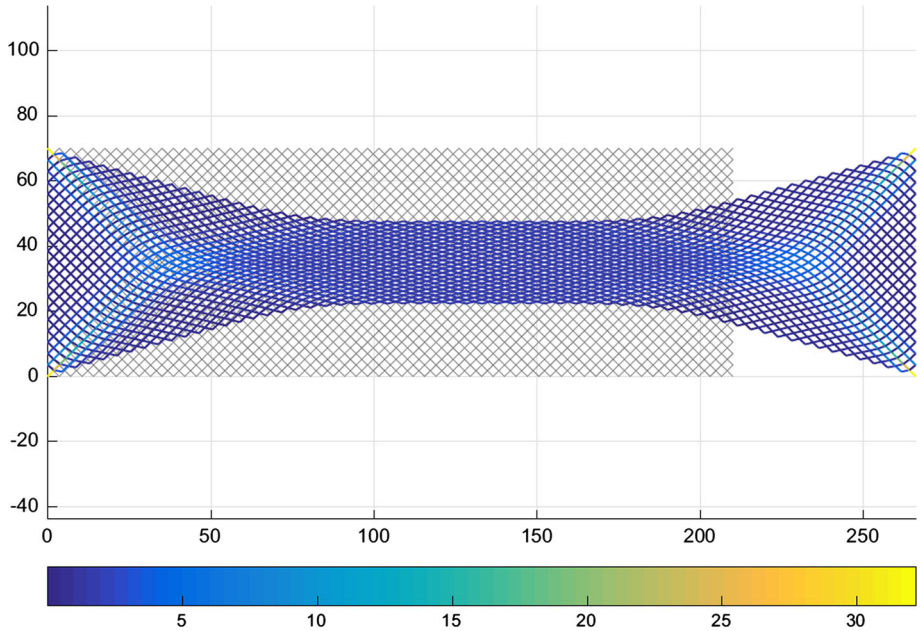

Fig. 12 Bias extension test simulation using the micromodel when $M = 20$ and $N = 60$: reference configuration (gray), current shape and color bar of the internal forces on extensional springs [43] (color figure online)

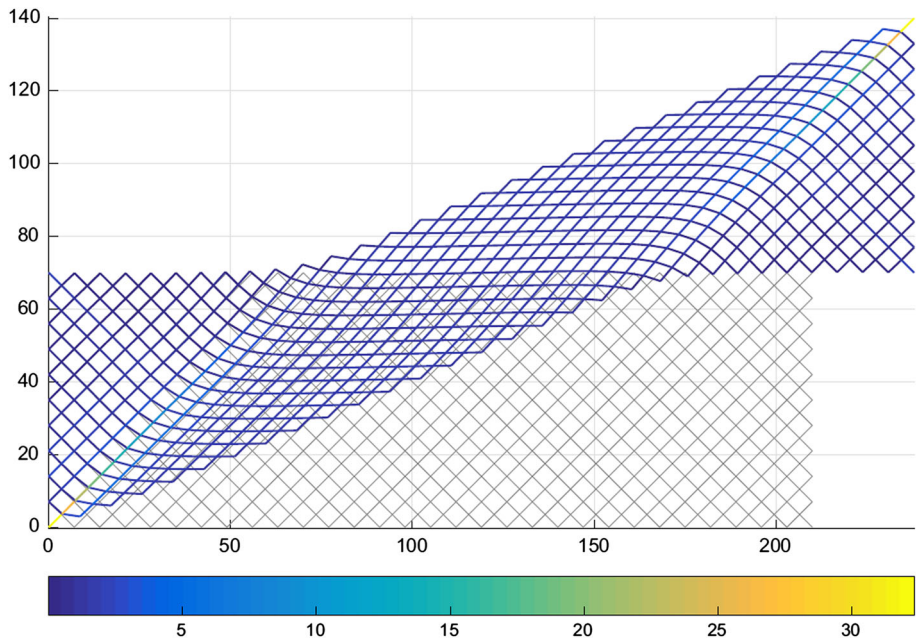

Fig. 13 Shear-extension test simulation using the micromodel: reference configuration (gray), current shape and color bar of the internal forces on extensional springs for $M = 10$ and $N = 30$ [43] (color figure online)

energy (16) is shown, along with colors indicating the magnitude of internal forces on extensional springs computed in the current configuration, and whose expression is given in Ref. [43]. In the same manner, in Fig. 13, the equilibrium shape resulting from a shear test simulation is shown.

1.4 À la Piola homogenized elastic plate model

Considering the discrete Hencky-type micromodel presented above, a $2D$ continuum macromodel has been derived by means of micro–macro transitions. Expanding in truncated Taylor series the kinematic map [13], the microplacement field of material particles at the nodes of the referential lattice is computed by means of the values, in such nodes, of a regular macro-placement and its first gradient. Such a map determines a unique micromotion once a macro-motion is given. The micro–macro transition is obtained by equating the microstrain energy with the macroscopic counterpart, thus obtaining a macroscopic Lagrangian surface density of strain energy in terms of the constitutive coefficients appearing in the postulated expression of the microstrain energy. Numerical simulations with both discrete and homogenized models show that the homogenized model is representative of the microscopic response [42,43]. Following the notation introduced above, we now consider a $2D$ continuum whose reference shape is given by a rectangular domain $\Omega = [0, N\epsilon] \times [0, M\epsilon] \subset \mathbb{R}^2$. Very often, it is assumed that $N = 3M$, which is the standard relation between the width and height of a fabric specimen for experimental and numerical tests. By assuming planar motions, the current shape of Ω is described by regular macro-placement $\boldsymbol{\chi} : \Omega \to \mathbb{R}^2$. The kinematic map providing the micro–macro identification is the so-called Piola ansatz and we accordingly choose $p_{i,j} = \boldsymbol{\chi}(P_{i,j}) \quad \forall i = 1, \dots, N, \ \forall j = 1, \dots, M$. Assuming that $\boldsymbol{\chi}(\cdot)$ is at least twice differentiable at $P_{i,j}$, the following 2nd-order approximations are obtained

$$\begin{aligned}
\|p_{i+1,j} - p_{i,j}\| &= \|\boldsymbol{\chi}(P_{i+1,j}) - \boldsymbol{\chi}(P_{i,j})\| \backsimeq \epsilon \|F(P_{i,j})D_1 + \frac{\epsilon}{2}\nabla F(P_{i,j})|D_1 \otimes D_1\| \\
\|p_{i,j+1} - p_{i,j}\| &= \|\boldsymbol{\chi}(P_{i,j+1}) - \boldsymbol{\chi}(P_{i,j})\| \backsimeq \epsilon \|F(P_{i,j})D_2 + \frac{\epsilon}{2}\nabla F(P_{i,j})|D_2 \otimes D_2\|
\end{aligned} \tag{15}$$

where F is the deformation gradient $\nabla\boldsymbol{\chi}$. The reader is referred to the original papers [13,42,43] for further details. Equation (15) have been used for the homogenization procedure of two addends of Eq. (14). In order to address the other three terms, the cosines of the angles $\vartheta^{\alpha}_{i,j}$ ($\alpha = 1, 2$) and $\vartheta^{3}_{i,j}$ are derived as functions of the macro-placement $\boldsymbol{\chi}$. Using analogous Taylor expansions as those in Eq. (15) neglecting $o(\epsilon^2)$ terms, and writing all quantities in terms of the displacement $\boldsymbol{\chi}$, the strain energy of the micromodel becomes

$$\begin{aligned}
U(\{p_{i,j}\}) = &\sum_j \sum_i \sum_\alpha \frac{k^{\alpha}_{i,j}}{2}\epsilon^2 (\|F(P_{i,j})D_\alpha + \frac{\epsilon}{2}\nabla F(P_{i,j})|D_\alpha \otimes D_\alpha\| - 1)^2 \\
&+ \sum_j \sum_i \sum_\alpha b^{\alpha}_{i,j} \left[\frac{\|\nabla F(P_{i,j})|D_\alpha \otimes D_\alpha\|^2}{\|F_{i,j}D_\alpha\|^2} - \left(\frac{F(P_{i,j})D_\alpha \cdot \nabla F(P_{i,j})|D_\alpha \otimes D_\alpha}{\|F_{i,j}D_\alpha\|^2} \right)^2 \right] \frac{\epsilon^2}{2} \\
&+ \sum_j \sum_i \frac{b^{3}_{i,j}}{2} \left| \arccos\left(\frac{F(P_{i,j})D_1 \cdot F(P_{i,j})D_2}{\|F(P_{i,j})D_1\| \cdot \|F(P_{i,j})D_2\|} \right) - \frac{\pi}{2} \right|^{\xi},
\end{aligned} \tag{16}$$

Rescaling the rigidities as

$$k^{\alpha}_{i,j} = \mathbb{K}^{\alpha}_{e}; \ b^{\alpha}_{i,j} = \mathbb{K}^{\alpha}_{b}; \ b^{3}_{i,j} = \mathbb{K}_{p}\epsilon^2 \tag{17}$$

and letting $\epsilon \to 0$, the strain energy of the macroscopic system reduces to

$$\begin{aligned}
U(\boldsymbol{\chi}(\cdot)) = &\int_\Omega \sum_\alpha \frac{\mathbb{K}^{\alpha}_{e}}{2} \|FD_\alpha - 1\|^2 \mathrm{d}S \\
&+ \int_\Omega \sum_\alpha \frac{\mathbb{K}^{\alpha}_{b}}{2} \left[\frac{\|\nabla F|D_\alpha \otimes D_\alpha\|^2}{\|FD_\alpha\|^2} - \left(\frac{FD_\alpha \cdot \nabla F|D_\alpha \otimes D_\alpha}{\|FD_\alpha\|^2} \right)^2 \right] \mathrm{d}S \\
&+ \int_\Omega \frac{\mathbb{K}_{p}}{2} \left| \arccos\left(\frac{FD_1 \cdot FD_2}{\|FD_1\| \cdot \|FD_2\|} \right) - \frac{\pi}{2} \right|^{\xi} \mathrm{d}S.
\end{aligned} \tag{18}$$

It is noteworthy that the shear strain introduced in the considered macromodel is different from that defined in the Pipkin continuum model [see Eq. (8)]. In Fig. 14, equilibrium shapes and their corresponding shear strains are compared for different (pure) shear test simulations (refer to problem 2 above) using the strain energy (18). Reference [18] has first addressed the homogenization à la Piola of pantographic fabrics in a linear setting, proving that the homogenization of pantographic fabrics gives rise to second gradient continua.

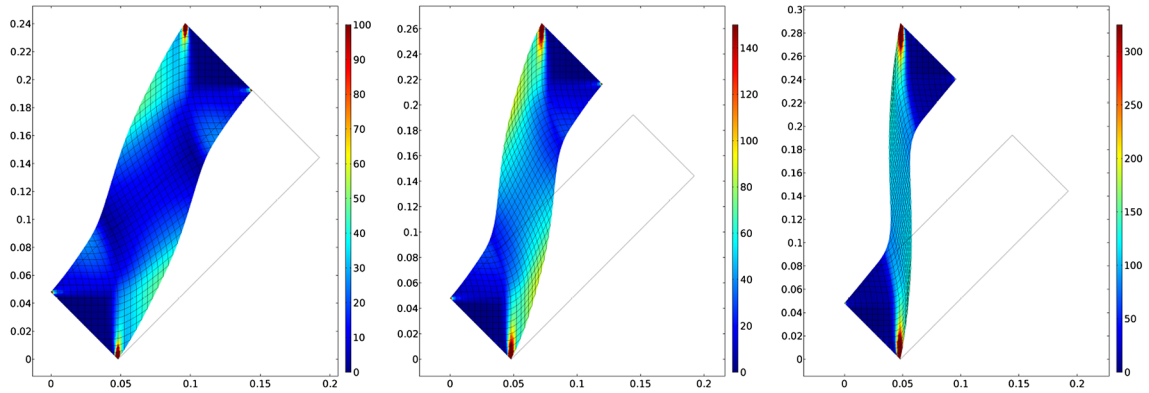

Fig. 14 Equilibrium shape and strain energy density when a shear displacement is prescribed [13] (color figure online)

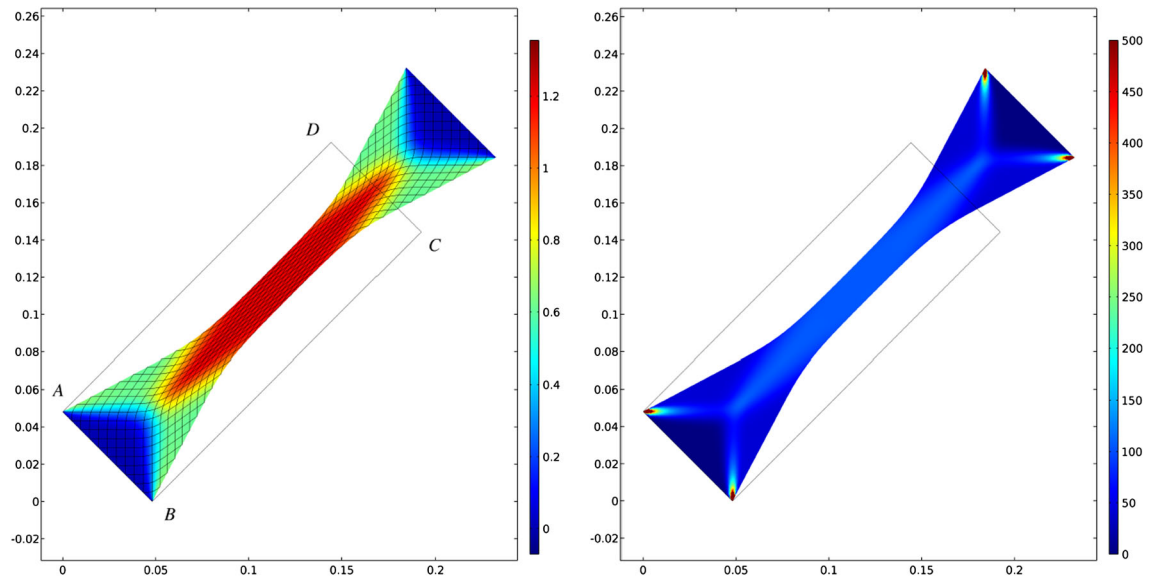

Fig. 15 Numerical simulation of the bias extension test. Colors indicate the shear strain relative to the initial fiber axes (left) and the strain energy density (right) [13]

Several numerical simulations show the presence of (internal) boundary layers, a hallmark of second gradient theories. In Fig. 15, numerical simulations of the bias extension test are shown. The colors indicate the shear strain relative to the initial fiber axes (left) and the strain energy density (right) [13]. In Fig. 16, color maps of the strain energy density are shown for standard bias extension test (left) and combined rotation-compression test (right) of a rectangular linear elastic specimen pantographic fabrics with holes.

The well-posedness of linearized equilibrium equations deriving from the stationarity of the energy functional (18), which is valid in the neighborhood of a stress free configuration for pantographic sheets, cannot be immediately studied by using the results available in the literature. It has been proven that the standard strategy involving the use of Poincaré inequality, Lax–Milgram Theorem, and coercivity of bilinear strain energy form also apply in the context of linear elastic pantographic sheets [44]. The key idea is the exploitation of an unusual energy space, where the solutions relative to well-posed boundary conditions are looked for. It is observed that the energy space of linear pantographic sheets, i.e., the space of functions fulfilling boundary conditions for which the strain energy is meaningful, is included in a special class of Sobolev spaces, the so-called Anisotropic Sobolev Space. The definition of Anisotropic Sobolev Space was conceived on purely logical grounds by Sergei M. Nikol'skii and has to be used in order to apply the abstract Hilbertian setting of solution strategy. Thus, in order to address the well-posedness of the planar linearized equilibrium problem for homogenized pantographic lattices, (1) a class of subsets of anisotropic Sobolev space is introduced as the most suitable energy space relative to assigned boundary conditions; (2) it is proved that the considered strain

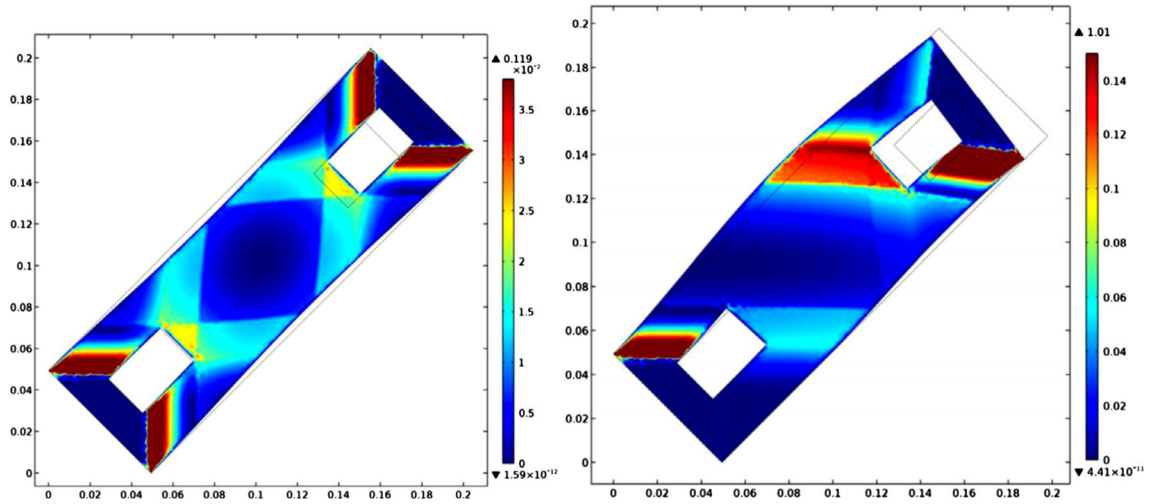

Fig. 16 Color maps of the strain energy density for standard bias extension test (left) and combined rotation-compression test (right) of rectangular linear elastic specimen pantographic fabrics with rectangular holes (color figure online)

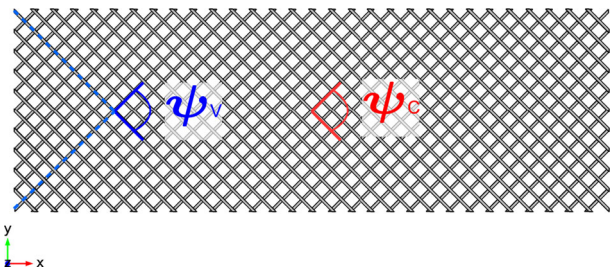

Fig. 17 Two control angles employed in the identification procedure

energy density is coercive and positive definite in such energy space; (3) the set of placements for which the strain energy is vanishing (the so-called floppy modes) must strictly include rigid motions; (4) the restrictions on displacement boundary conditions that ensure the existence and uniqueness of linear static problems are determined.

1.5 Numerical identification of homogenized model

In Ref. [42], the parameters $\mathbb{K}_a^\alpha$, $\mathbb{K}_b^\alpha$ and $\mathbb{K}_p$ appearing in the strain energy are assumed to be independent of the position and family of beams they are related to and the strain energy density of the homogenized model (18). The parameter identification is numerical, which means that the constitutive parameters $\mathbb{K}_e$, $\mathbb{K}_b$ and $\mathbb{K}_p$ of the homogenized model are calibrated by means of several numerical computations performed with the 3D Cauchy model of isotropic and homogeneous elastic materials undergoing arbitrarily large strains. Several bias extension test simulations [45] using both the standard Cauchy model and the higher gradient model, for several displacements prescribed on the shorter side of the specimen, are performed. For each simulation, the overall stored energy and two representative deformations at specific points are evaluated. The two representative deformations are chosen to be the angles ψ_C and ψ_V, evaluated at the probed points shown in Fig. 17, i.e., at the center C of the specimen and at the corner V of the "quasi-rigid" triangle near a base of the specimen.

The material parameters of the macromodel $\mathbb{K}_e$, $\mathbb{K}_b$ and $\mathbb{K}_p$ are estimated by minimizing the squared errors for the overall stored energy and the two angles ψ_C, ψ_V, when computed with both the homogenized and Cauchy models. The two angles ψ_C, ψ_V have been chosen among other possible control quantities because each of them is strongly related to one of the last two energy terms (18) only dependent only on one parameter each. The energy involved in the distortion angle at the center is mostly governed by the parameter $\mathbb{K}_p$, while the distortion angle at the triangle vertex depends for the most part on the bending energy related to $\mathbb{K}_b$, thus allowing to easily find the minimum of the squared error for the two angles by separately tuning $\mathbb{K}_e$ and $\mathbb{K}_b$. The

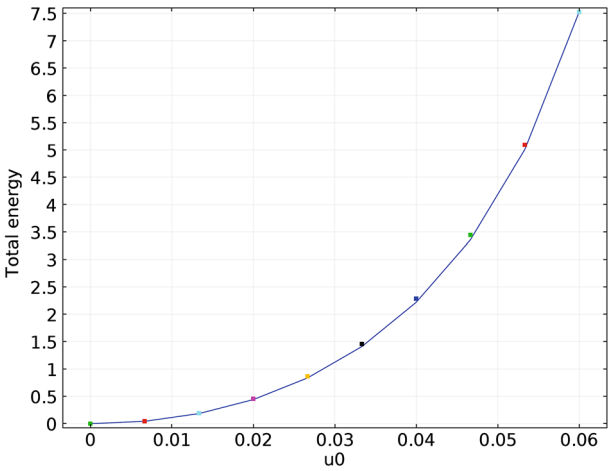

Fig. 18 Comparison of the total energy between the Cauchy model (points) and the second gradient model (solid line)

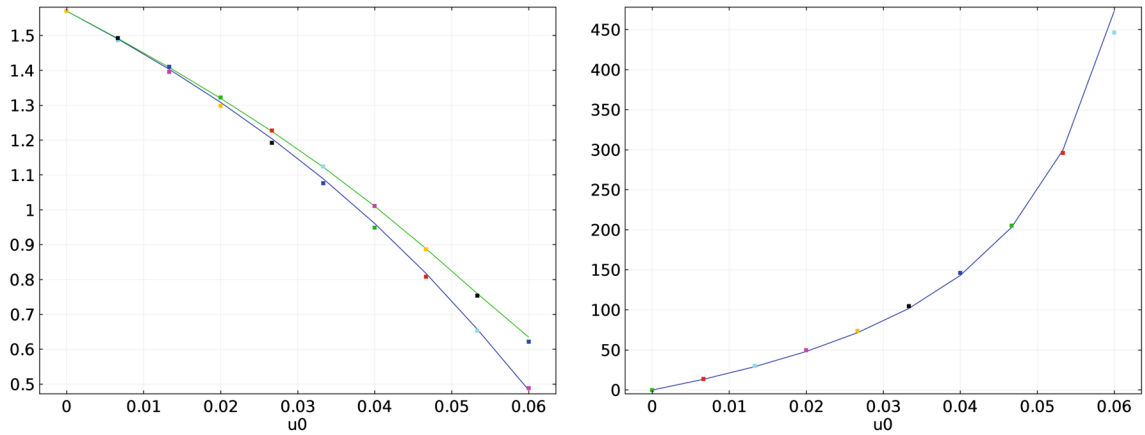

Fig. 19 Comparisons between the Cauchy model (points) and the regression with the second gradient model (solid line). **a** Angle at the center ψ_C (blue line) and angle at the corner ψ_V (green line) on the left; **b** total reaction force (color figure online)

last parameter $\mathbb{K}_e$ is derived by considering the whole stored energy. In Figs. 18 and 19 (left), the total energy and the angles ψ_C and ψ_V used for fitting the second gradient model are shown as the prescribed displacement in the bias extension test is varying. In Fig. 19 (right), a comparison between the total reaction force of the micromodel and the one evaluated with the macromodel is plotted versus the prescribed displacement. This quantity was computed by means of Castigliano's first theorem. Figure 20 shows that for the Cauchy model a non-negligible amount of energy is stored for configurations that are not accounted for in the coarser second gradient model. The main reason is that the Cauchy model has a richer kinematics than the homogenized one. Figure 19 (right) confirms this statement that at large displacements, which are likely to be those where strain energies due to the richer kinematics of the refined model start to gain significance.

1.6 Elastic surface models

In Ref. [46], the formulation of a model for pantographic sheets, which is regarded as elastic surfaces embedded in a three-dimensional Euclidean space, has been first presented. In order to account for the geodesic (thus generalizing the classical plate theory) and out-of-plane bending of fibers, the model exhibits an associated second gradient areal strain energy density, which depends on the first and second gradients of the deformation. Accounting for the fact that fibers are arranged in two material directions, a Lagrangian Cartesian orthonormal coordinate system, whose associated basis of unit vectors is (D_1, D_2), is introduced in the reference config-

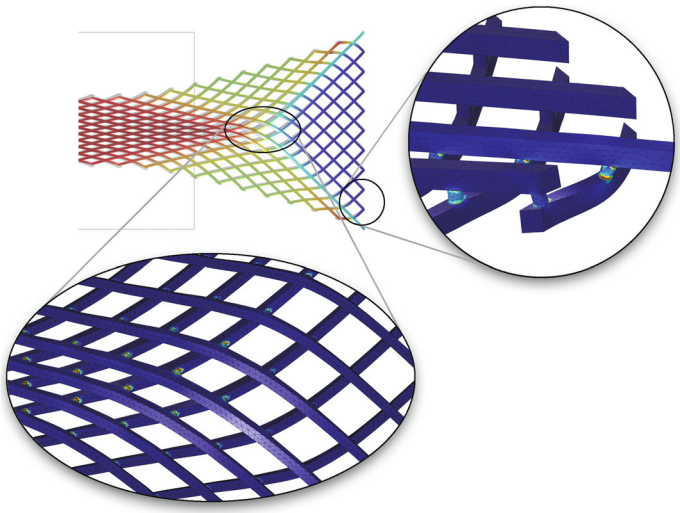

Fig. 20 3D deformation details; the colors in the zooms indicate qualitatively the stored elastic energy density for the 3D Cauchy model (color figure online)

uration. We now consider a $2D$ continuum, whose reference shape is the rectangular domain $\mathscr{B} \subset \mathbb{R}^2$. As customary, D_1 and D_2 are defined as the push-forward vectors in the current configuration of the vectors D_1 and D_2, respectively, i.e., $D_\alpha = FD_\alpha,\ \alpha = 1, 2$. In the sequel fiber, stretches $\|D_\alpha\|$ are denoted as λ and μ

$$F = D_1 \otimes D_1 + D_2 \otimes D_2 = \lambda \tilde{D}_1 \otimes D_1 + \mu \tilde{D}_2 \otimes D_2 \tag{19}$$

where $\tilde{D}_\alpha = \frac{D_\alpha}{\|D_\alpha\|}$ are the unit vectors associated with D_α. Such vectors are used to define the fiber shear strain γ as $\sin\gamma = \tilde{D}_1 \cdot \tilde{D}_2$ [13,46]. The shear strain introduced in this model is different from that defined in the Pipkin continuum model [10,34,35]. From Eq. (19), the right Cauchy-Green tensor reads

$$C = F^{\mathsf{T}}F = \lambda^2 D_1 \otimes D_1 + \mu^2 D_2 \otimes D_2 + \lambda\mu \sin\gamma\, (D_1 \otimes D_2 + D_2 \otimes D_1)\,. \tag{20}$$

and

$$Jn = FD_1 \times FD_2 = D_1 \times D_2 \tag{21}$$

with n the unit normal of the deformed surface field and $J = \lambda\mu|\cos\gamma|$ the local areal dilation due to the deformation. In Ref. [46], the following representation formula is proven

$$\nabla\nabla\boldsymbol{\chi} = (g_1 + K_1 n) \otimes D_1 \otimes D_1 + (g_2 + K_2 n) \otimes D_2 \otimes D_2 + (\boldsymbol{\Gamma} + Tn) \otimes (D_1 \otimes D_2 + D_2 \otimes D_1) \tag{22}$$

with

$$g_1 = \lambda\eta_1 p + (D_1 \cdot \nabla\lambda)\, \tilde{D}_1;\ \ g_2 = \mu\eta_2 q + (D_2 \cdot \nabla\mu)\, \tilde{D}_2 \tag{23}$$

$$\boldsymbol{\Gamma} = (D_1 \cdot \nabla\mu)\, \tilde{D}_2 + \lambda\mu\phi_1 q = (D_2 \cdot \nabla\lambda)\, \tilde{D}_1 + \lambda\mu\phi_2 p \tag{24}$$

$$q = n \times \tilde{D}_2;\ \ p = n \times \tilde{D}_1 \tag{25}$$

$$K_1 = \lambda^2\kappa_1;\ \ K_2 = \mu^2\kappa_2;\ \ T = \lambda\mu\tau. \tag{26}$$

where η_1 and η_2 are the geodesic curvatures of the deformed fibers, ϕ_1 and ϕ_2 the so-called Tchebychev curvatures, κ_1 and κ_2 the normal curvatures of the deformed fibers, and τ measures the twist of the deformed surface. In Ref. [46], explicit expressions for geodesic and Tchebychev curvatures are provided

$$\begin{aligned}
J\eta_1 &= D_1 \cdot \nabla(\mu \sin\gamma) - D_2 \cdot \nabla\lambda \\
J\eta_2 &= D_1 \cdot \nabla(\mu) - D_2 \cdot \nabla(\lambda \sin\gamma) \\
J\phi_1 &= J\eta_2 + \lambda D_2 \cdot \nabla(\sin\gamma) \\
J\phi_2 &= J\eta_1 + \mu D_1 \cdot \nabla(\sin\gamma).
\end{aligned}$$

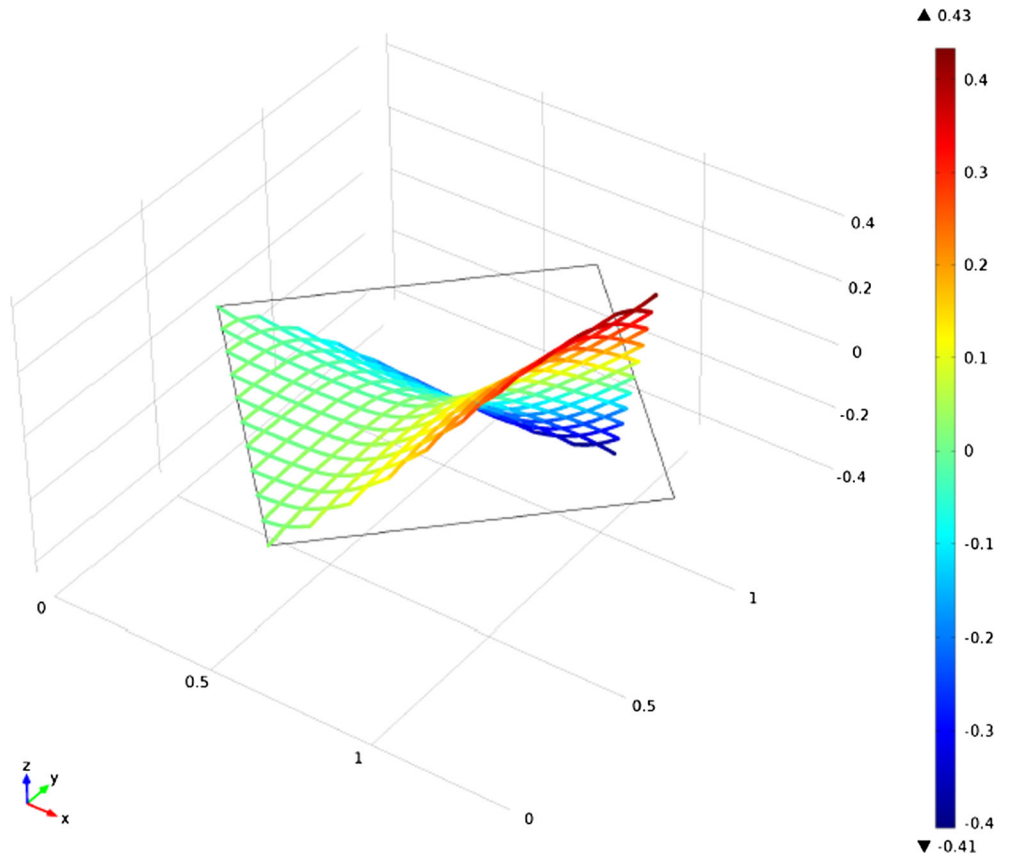

Fig. 21 Numerical simulation of torsion of a square sheet ($\theta = 60°$) using the elastic surface model presented above. Colors represent qualitatively the out-of-plane component of the displacement u_3 (color figure online)

Furthermore, a strain energy density function, which depends on the first and second gradients of the deformation and incorporating the orthotropic symmetry conferred by the reference fiber arrangement, can be proposed [47]

$$W = w(\lambda, \mu, J) + \frac{1}{2}\left(A_1|g_1|^2 + A_2|g_2|^2 + A_\Gamma|\boldsymbol{\Gamma}|^2 + k_1K_1^2 + k_2K_2^2 + k_TK_T^2\right) \tag{27}$$

where $A_1,\ A_2,\ A_\Gamma,\ k_1,\ k_2,\ k_T$ are constitutive constants. In Fig. 21, numerical simulations of the torsion of a square sheet using the elastic surface model presented above are shown. Many fiber reference curvatures have been considered (e.g., sinusoidal, spiral, parabolic fibers), and for parabolic fibers, experiments (Fig. 22) and model (Fig. 23) both show that, after a critical load, out-of-plane buckling occurs during bias extension, because the transverse (curved) beams in the middle of the specimen undergo buckling induced by the shortening of the middle width of the specimen.

A 2D continuum model embedded in a 3D space has been also proposed [48] where, relying on a variational framework, the following strain energy density is proposed

$$\begin{aligned}\pi = \frac{1}{2}\Big\{ & K_e\left[\left(\epsilon^1\right)^2 + \left(\epsilon^2\right)^2\right] + K_s\gamma^2 + \\ & + K_t\left[\left(\kappa_1^1\right)^2 + \left(\kappa_1^2\right)^2\right] + K_n\left[\left(\kappa_2^1\right)^2 + \left(\kappa_2^2\right)^2\right] + K_g\left[\left(\kappa_3^1\right)^2 + \left(\kappa_3^2\right)^2\right]\Big\}\end{aligned} \tag{28}$$

It corresponds to a system of two orthogonal continuous families "1" and "2" of straight shear-undeformable beams arranged along the coordinate axes in the reference configuration and resembling the pantographic microstructure. The fibers of family α are parallel to the direction $\hat{e}_\alpha$. The contributions $\frac{1}{2}K_e\left(\epsilon^1\right)^2$ and

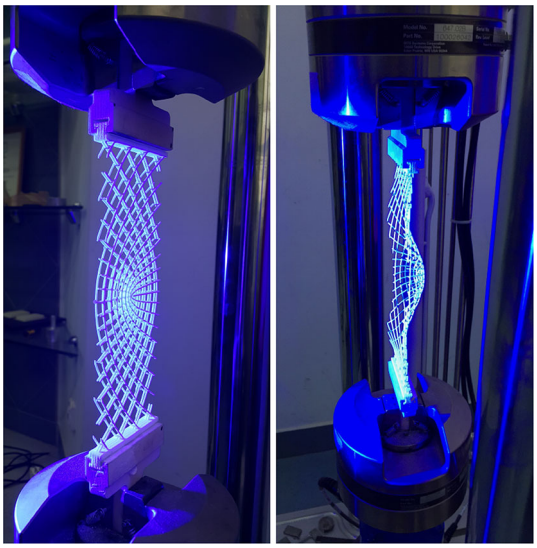

Fig. 22 Bias extension test on parabolic pantographic fabric. Out-of-plane buckling is observed after critical loading

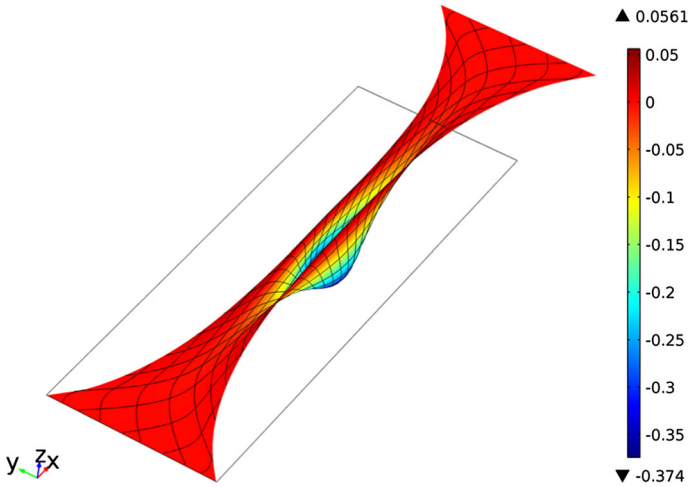

Fig. 23 Simulation of bias extension test on parabolic pantographic fabrics. Out-of-plane buckling is observed after a critical loading. Deformed configuration and qualitative out of plane displacement

$\frac{1}{2}K_e\left(\epsilon^2\right)^2$ stand for the elongation of fibers belonging to, respectively, the families "1" and "2." The strain measure $\boldsymbol{\epsilon}^\alpha$, with $\alpha = 1, 2$, is defined as

$$\epsilon^\alpha = \left\| \frac{\partial \chi}{\partial X_\alpha} \right\| - 1 \tag{29}$$

and $K_e \in [0, \infty)$ is the corresponding stiffness, which is assumed to be the same for both families of fibers. The contribution $K_s\gamma^2$ is accounting for the shear deformation of the sheet, i.e., it is due to the relative rotation of two orthogonal intersecting fibers. It represents the strain energy stored in the pivot because of its torsion of angle γ. The strain measure $\gamma \in [-\frac{\pi}{2}, \frac{\pi}{2}]$, also referred to as the shear angle, is expressed as

$$\gamma = \arcsin \frac{\frac{\partial \chi}{\partial X_1} \cdot \frac{\partial \chi}{\partial X_2}}{\left\| \frac{\partial \chi}{\partial X_1} \right\| \left\| \frac{\partial \chi}{\partial X_2} \right\|} \tag{30}$$

and $K_s$is a positive constitutive parameter. The terms $\frac{1}{2}\left[K_t\left(\kappa_1^1\right)^2 + K_n\left(\kappa_2^1\right)^2 + K_g\left(\kappa_3^1\right)^2\right]$ and $\frac{1}{2}\left[K_t\left(\kappa_1^2\right)^2 + K_n\left(\kappa_2^2\right)^2 + K_g\left(\kappa_3^2\right)^2\right]$ are due to twist, normal bending and geodesic bending of beams belonging, respec-

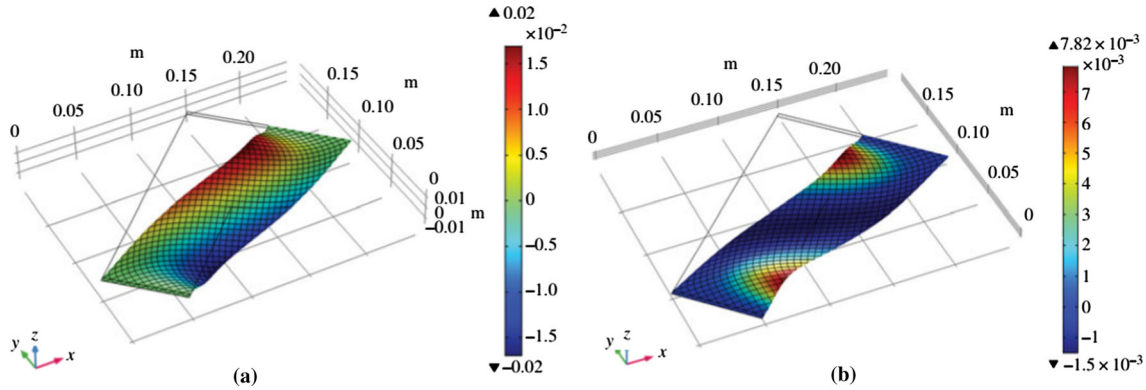

Fig. 24 Shear test. Qualitative buckled shapes of the first two bifurcation modes. Colors indicate values of the out-of-plane displacement. **a** First and **b** second buckling modes (color figure online)

tively, to families "1" and "2" of fibers. The strain measures $\kappa_1^\alpha, \kappa_2^\alpha, \kappa_3^\alpha$ are the coordinates, in the augmented levorotatory reference Cartesian frame, of the axial vector corresponding to the skew tensor $W^\alpha = (R^\alpha)^{\mathrm{T}} \frac{\partial R^\alpha}{\partial X_\alpha}$, which is the so-called current curvature tensor. The orthogonal tensor R^α transforms the augmented levorotatory reference Cartesian frame vectors into the following ordered triplet: (1) the unitary vector tangent to the deformed coordinate line α; (2) the unitary vector normal to the previous one and lying in the plane tangent to the deformed surface; (3) the unitary vector normal to the plane tangent to the deformed surface. Explicit (lengthy) derivations can be found in Ref. [48].

It is worth noting that (1) since the beams are assumed to be shear-undeformable (2) both R^1 and R^2 transform the third vector $\hat{e}_3$ of the augmented levorotatory reference Cartesian frame into the same vector, (3) assuming that principal inertia axes of the cross sections for the two families "1" and "2" of beams in the undeformed configuration are considered to be, respectively, $(\hat{e}_2, \hat{e}_3)$ and $(-\hat{e}_1, \hat{e}_3)$, the cross sections of the beams belonging to the two families "1" and "2" are eigen-inertia vectors in the deformed configuration the unitary vectors of points (2) and (3) above and, hence, they share the second principal inertia axis at point (3) above. Such vector is also interpreted as the current axis of the elastic cylindrical pivot. This means that deformation modes of the pivots other than their torsion are kinematically excluded in this model, i.e., the pivots are assumed to remain orthogonal to both fibers in the current configuration and only their torsion contributes to the strain energy. Further, κ_1^α, κ_2^α, κ_3^α can also be interpreted as geodesic torsion, normal curvature and geodesic curvature of the deformed surface multiplied, respectively, by $\| \frac{\partial \chi}{\partial X_\alpha} \|$, since X_α is not a unitary speed parameterization. Last, the fibers intersecting in one point cannot detach or have a relative displacement, since their motion is described by the same placement function. (This is not a so-called mixture model.) Using the above model, shear test simulations have been performed reporting the occurrence of out-of-plane buckling (Fig. 24).

1.7 Analytical identification of elastic plate models

Let us consider a two-dimensional body, whose points can be put in a bijective correspondence with a closed subset $\mathcal{B}$ of the Euclidean space $\mathbb{R}^2$. The set $\mathcal{B}$ represents the shape of the body in the reference (undeformed) configuration. A Cartesian coordinate system $(\mathcal{O}, (\hat{e}_1, \hat{e}_2))$ is introduced, with $X = (X_1, X_2)$ the coordinates of the generic point in the Euclidean space $\mathbb{R}^2$.

Working in a Lagrangian framework, a placement function $\chi : \mathcal{B}_0 \to \mathbb{R}^2$ such that the image $x = \chi(X)$ of X through χ is the current position of point X. The displacement field $u : \mathcal{B}_0 \to \mathbb{R}^2$ is defined as $u(X) = \chi(X) - X$. The placement, or equivalently the displacement, is the independent kinematic descriptor of the system. The image $\mathcal{B} = \chi(\mathcal{B})$ of $\mathcal{B}$ through χ is the current shape of the body. Let $F = \nabla_X \chi$ be the gradient (with respect to the Lagrangian coordinate X) of the placement function χ. The tensor F belongs to Lin^+, the group of second order tensors with positive determinant, i.e., orientation preserving. An objective strain measure $G = \left[F^T F - I\right]/2$ (Green-Lagrange strain tensor) is then defined. Henceforth, the subscript X will be omitted in ∇_X and each space derivative will be considered a material derivative. When the strain

energy density $\hat{U}(G, \nabla G)$ is considered to be depending quadratically upon the deformation tensor G and its gradient ∇G, the following representation formula applies [49]

$$\hat{U}^{\text{strain}} = \frac{1}{2}\epsilon^T C_{3\times 3}\epsilon + \frac{1}{2}\eta^T A_{6\times 6}\eta \tag{31}$$

with

$$\epsilon = \left(G_{11}\ G_{22}\ \sqrt{2}G_{12}\right)^{\mathrm{T}} \tag{32}$$

and

$$\eta = \left(G_{11,1}\ G_{22,1}\ \sqrt{2}G_{12,2}\ G_{22,2}\ G_{11,2}\ \sqrt{2}G_{12,1}\right)^{\mathrm{T}} \tag{33}$$

In order to account for anisotropy of the material, we must assume invariance of the strain energy density under the action, on the Cartesian coordinate system $\mathcal{O}, (\hat{e}_1, \hat{e}_2)$ labeling points of the reference configuration, of some symmetry group S of transformations, which could be any subgroup of *Orth*. When the symmetry group is the dihedral group D4 (orthotropic material), the representations for the matrices $C_{3\times 3}$ and $A_{6\times 6}$ read

$$C^{D4}_{3\times 3} = \begin{pmatrix} c_{11} & c_{12} & 0 \\ c_{12} & c_{22} & 0 \\ 0 & 0 & c_{33} \end{pmatrix} \tag{34}$$

and

$$A^{D4}_{6\times 6} = \begin{pmatrix} A^{D4}_{3\times 3} & 0 \\ 0 & A^{D4}_{3\times 3} \end{pmatrix} \tag{35}$$

with c_{11} and c_{12} in $C^{D4}_{3\times 3}$ corresponding to the two Lamé coefficients

$$A^{D4}_{3\times 3} = \begin{pmatrix} a_{11} & a_{12} & a_{13} \\ a_{12} & a_{22} & a_{23} \\ a_{13} & a_{23} & a_{33} \end{pmatrix} \tag{36}$$

In Refs. [50–52], compatible identifications of the constitutive parameters appearing in Eq. (31) have been carried out, thus completely characterizing the set of constitutive parameters in terms of the fiber base material parameters (i.e., Young's modulus), of the fiber cross section parameters (i.e., area and moment of inertia), and of the distance between the nearest pivots. In particular, the constitutive parameters have been identified in the small strain case $|\nabla u| \ll 1$, modeling fibers as (geometrically linear) Euler–Bernoulli beams and pivots as rotational (elastic) springs with a quadratic potential in the relative rotation (torsion of pivots) angle between fibers belonging to two different families. The following expressions for the matrices $C^{D4}_{3\times 3}$ and $A^{D4}_{3\times 3}$ are the outcome of the investigation [52]

$$C^{D4}_{3\times 3} = \begin{pmatrix} \frac{EA}{d} & 0 & 0 \\ 0 & \frac{EA}{d} & 0 \\ 0 & 0 & 2k_R \end{pmatrix} \tag{37}$$

$$A^{D4}_{3\times 3} = \frac{EI}{d}\begin{pmatrix} 0 & 0 & 0 \\ 0 & 1 & -\sqrt{2} \\ 0 & -\sqrt{2} & 2 \end{pmatrix} \tag{38}$$

with E, A and I being, respectively, the Young's modulus, the cross-sectional area and the inertia moment of the cross section of beams, and d being the spacing between adjacent beams. Finally, k_R is the equivalent elastic torsional stiffness of the cylindrical pivots. The shear strain relative to the directions v and w is defined as (with $-\frac{\pi}{2} < \gamma < \frac{\pi}{2}$)

$$\sin\gamma = \cos\left(\frac{\pi}{2} - \gamma\right) = \frac{Fv \cdot Fw}{\|Fv\|\ \|Fw\|} = \frac{w^T F^T F v}{\|Fv\|\ \|Fw\|} = \frac{w^T\ (2G + I)\ v}{\|Fv\|\ \|Fw\|}. \tag{39}$$

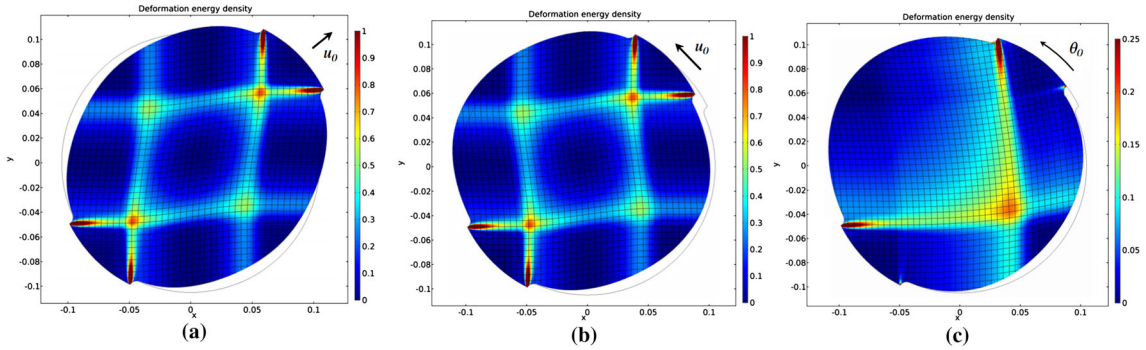

Fig. 25 Circular pantographic specimen. Qualitative color maps of the strain energy density for: bias extension test (**a**), shear test (**b**), rotation test (**c**)

In the present case $w = \hat{e}_1$ and $v = \hat{e}_2$. Thus, assuming that $-\frac{\pi}{2} \leq \gamma \leq \frac{\pi}{2}$

$$\gamma = \arcsin\left(\frac{2G_{12}}{\sqrt{\left(1+u_{1,1}\right)^2 + u_{2,1}^2}\sqrt{\left(1+u_{2,2}\right)^2 + u_{1,2}^2}}\right). \tag{40}$$

In the case of small strains, i.e., geometrically linear case $|\nabla u| \ll 1$

$$\gamma \simeq \arcsin\left(u_{1,2} + u_{2,1}\right) \simeq u_{1,2} + u_{2,1}. \tag{41}$$

Equation (31) yields the following remarkable expression for the strain energy density

$$\hat{U}^{\text{strain}} = \underbrace{\frac{1}{2}k_R\left(u_{1,2}+u_{2,1}\right)^2}_{\text{shear (pivot torsion) contribution}} + \underbrace{\frac{EA}{2d}\left(u_{1,1}^2+u_{2,2}^2\right)}_{\text{extension of fibers}} + \underbrace{\frac{EI}{2d}\left(u_{1,22}^2+u_{2,11}^2\right)}_{\text{bending of fibers}} \tag{42}$$

In Ref. [50], numerical solutions using the strain energy density (42) are presented for a circular pantographic specimen and three exemplary problems: bias extension, shear, and rotation tests (Fig. 25).

In Ref. [53], two pantographic sheets with an aspect ratio 3:1 are considered, having (1) the same fiber directions and (2) a part of their common sides interconnected by terminal clamping constraints, i.e., the displacements in the interconnected regions are pointwise equal for the two pantographic sheets. In the region corresponding to the cut separating the two sheets, no kinematic constraint is assumed for their relative displacement and the results shown in Fig. 26 are obtained for a standard bias extension test. Pantographic sheets without any internal cut are considered as well, see Fig. 27, where Eulerian representations of the strain energy densities are given for two nonstandard bias extension tests and in presence (absence) of the shear energy contribution. In particular in the first (higher) two plots in Fig. 27 the left side of the specimen have been clamped and the other sides are free, while the vertices of the right side are displaced along the direction of the longer sides. Instead, in the lower two plots, the left side of the specimen has been clamped and the lower half of the right side has been displaced along the direction of the longer sides, while the remaining boundaries are free. Second gradient energies allow for external actions on 2D continua not only on edges, but also on vertices, as vertex boundary conditions and vertex-forces.

1.8 Wave propagation in discrete arrangements of Euler beams

In Ref. [54], a model for studying the dynamics of pantographic fabrics has been introduced and subsequently employed [55,56]. Pantographic rectangular "long" waveguides are studied and time-dependent boundary displacements inducing the onset of traveling waves are considered. In this model, the two families of orthogonal fibers are regarded as two families of $1D$ orthogonal straight continua arranged in a rectangle in the reference configuration. Each continuum $\mathcal{C}_i$ has a standard linearized Euler elastic potential given by

$$U_i = \frac{1}{2}\int_{\mathcal{C}_i} k_M\left(u''(s)\right)^2 + k_N\left(w'(s)\right)^2 \mathrm{d}s \tag{43}$$

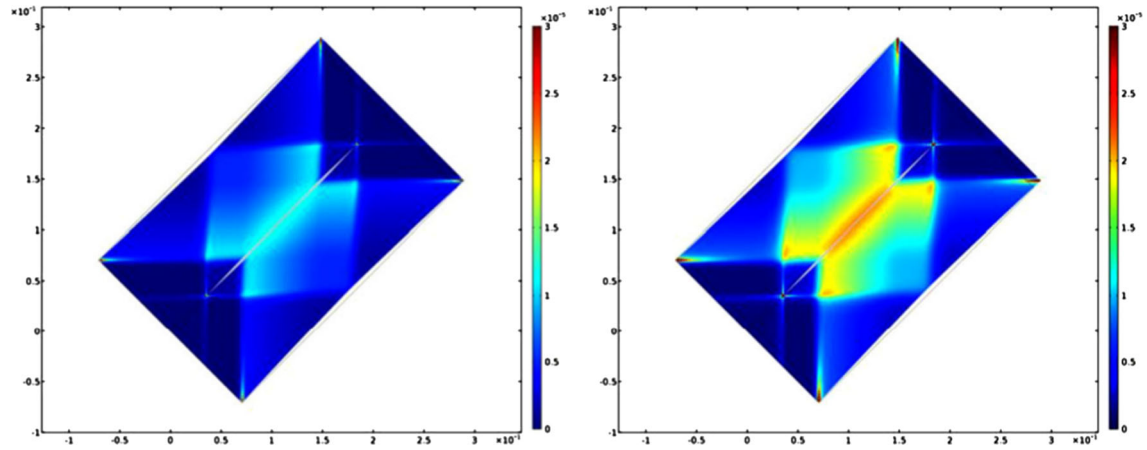

Fig. 26 Effect of a cut inside a sheet. Eulerian representation of the elastically stored energy density for a sheet with lower shear stiffness (left) and for a sheet with higher shear stiffness (right), both subject to a standard bias extension test

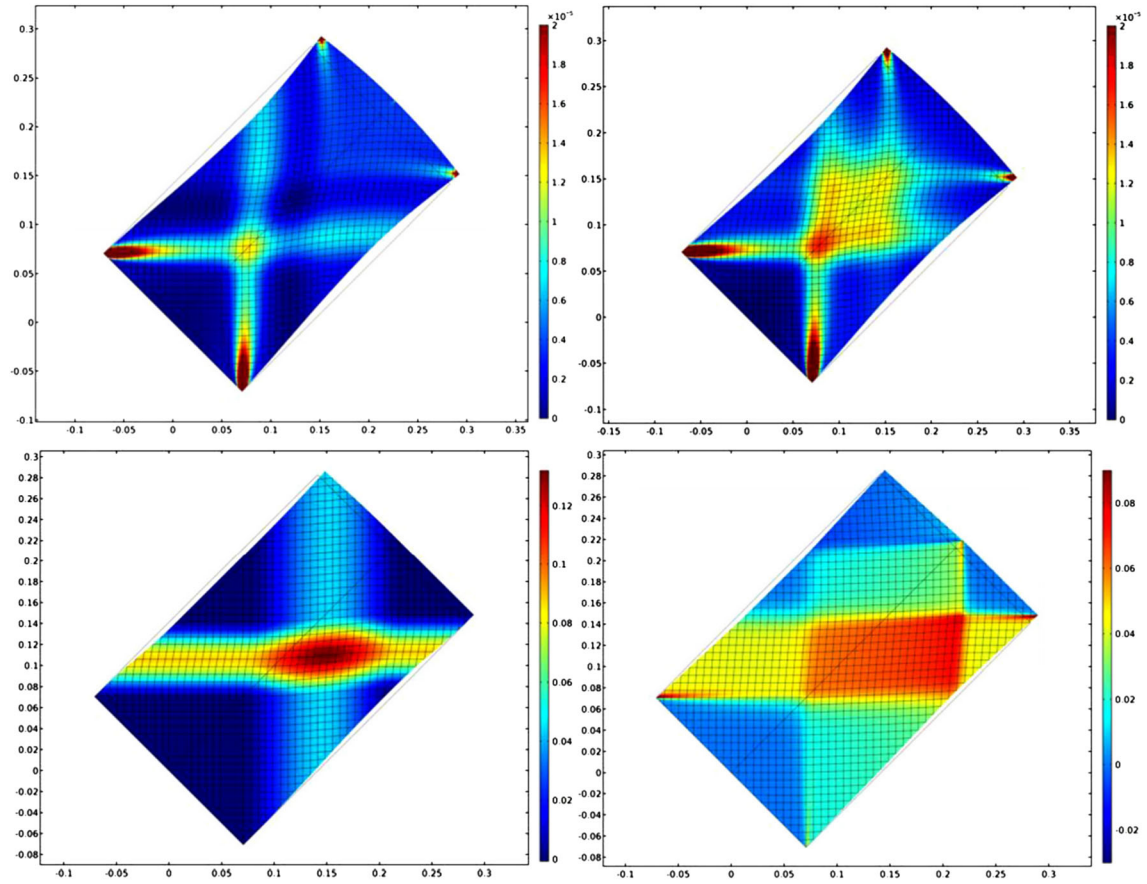

Fig. 27 Nonstandard bias extension test: Eulerian representation (including deformed shape and deformed sampled material lines) of the strain energy density for a sheet whose expression does not include the shear contribution (left) and for a sheet whose strain energy includes the shear contribution (right)

with s an abscissa introduced on each $\mathcal{C}_i$, k_M the bending stiffness, k_N the axial stiffness, u and w, respectively, the transverse and axial displacements. Dots in Fig. 28 (left) indicate the presence of frictionless hinges that do not interrupt the continuity of the beams. The displacement prescribed on the structure is an impulse function $\mathfrak{I} = u_0 * \operatorname{sech}[\tau(t - t_0)]$, with τ being a parameter affecting the duration of the pulse [Fig. 28 (right)].

In Fig. 29 (left) plots of the deformed shape of a pantographic strip during the propagation of a wave generated by a vertical impulse, uniformly applied on the upper side of the specimen while its lower side

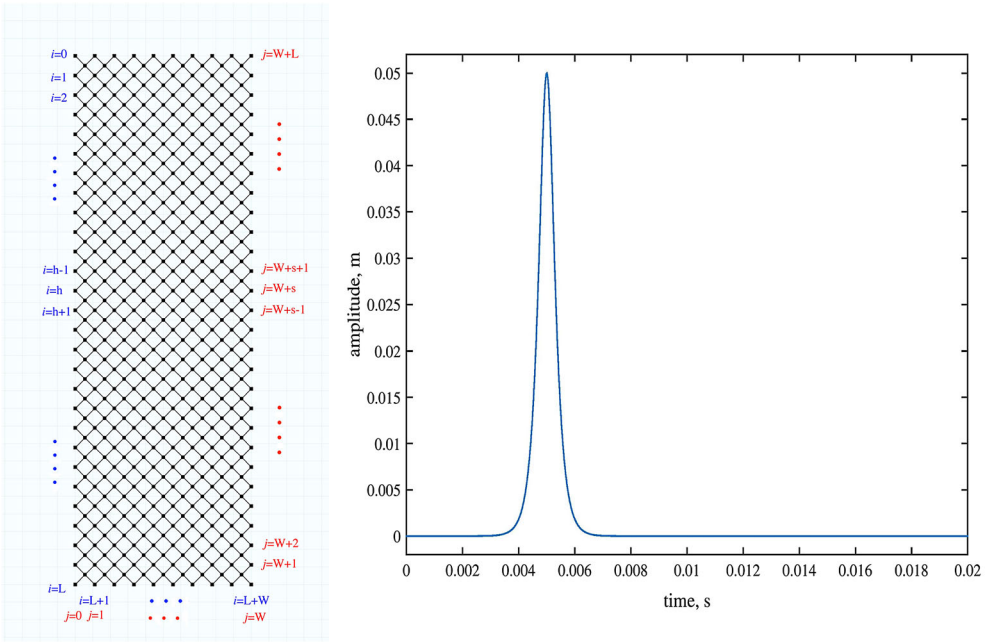

Fig. 28 Reference configuration (left) and time history of the impulse (right)

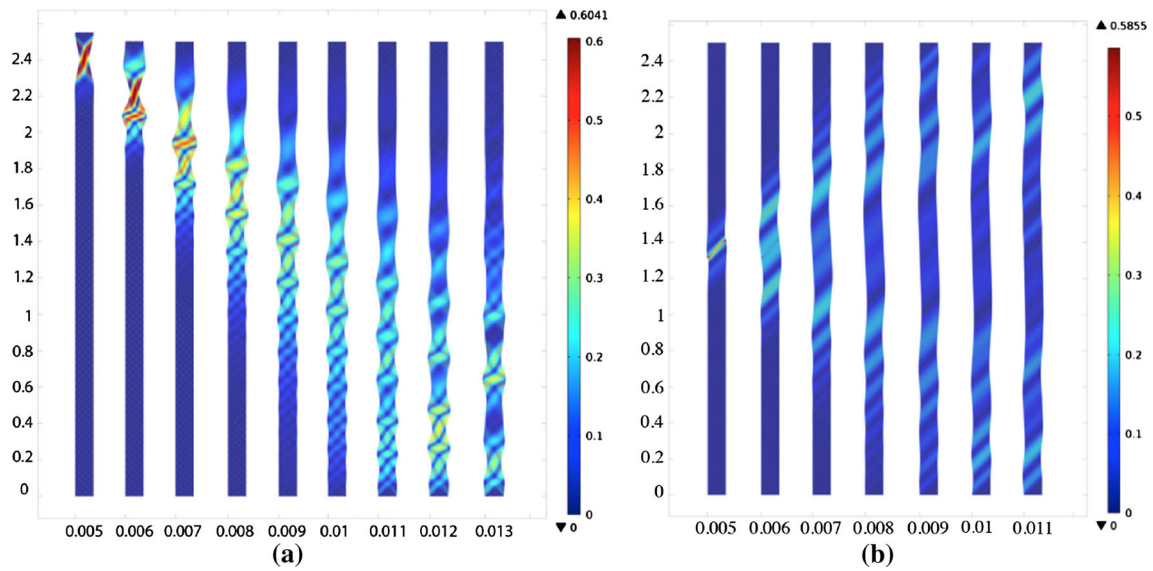

Fig. 29 Qualitative displacement plot of a wave propagating after a prescribed vertical displacement on the upper side (left). Wave propagating after double impulse (right)

remains clamped, are shown. Colors represent the magnitude of the total rotation of the cross section of the beams. In Fig. 29 (right), plots of the deformed shape of a pantographic strip during the propagation of a wave, generated by a double impulse applied at the middle height of the specimen, are shown, along with colors representing the magnitude of the total rotation of the cross section of the beams. By double impulse, we mean a couple of displacements, having the same orientation but opposite directions, oriented in one of the two orthogonal characteristic directions of the pantographic sheet. Such displacements are prescribed on two points at the opposite ends of two adjacent beams, i.e., consecutive beams belonging to the same orthogonal family of $1D$ continua, and their amplitude over time is shown in Fig. 28.

Such a double impulse corresponds, in the continuous homogenized limit case, to a double force, i.e., to a pair of forces with null resultant and moment. Figure 30 shows that the energy of the system remains

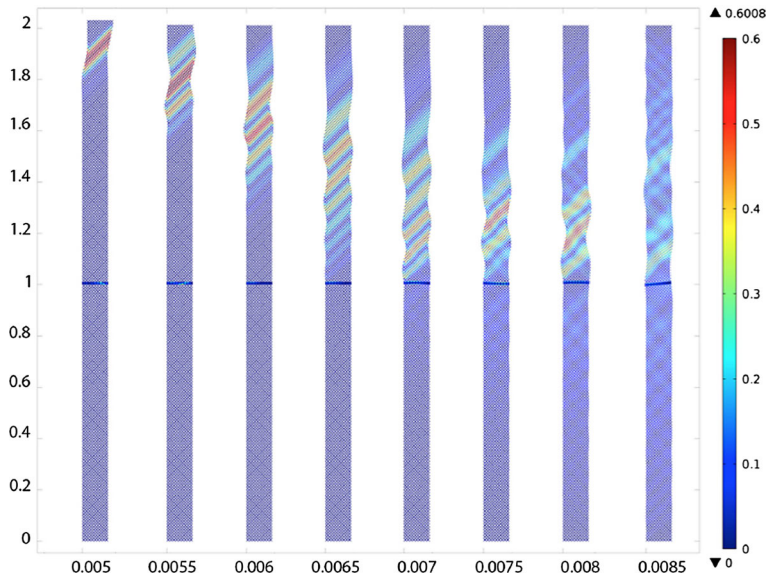

Fig. 30 Qualitative displacement of wave propagation in two identical lattices connected by an array of vertical beams

substantially confined in the upper half of the waveguide and propagation of waves beyond the discontinuity is negligible. Therefore, such type of discontinued pantographic structures induces damping.

2 Damage and failure in pantographic fabrics

So far the study of damage mechanisms in pantographic fabrics has been addressed from a modeling standpoint [57,58]. Further experimental data can be found [10,59]. In Ref. [57], in the aforementioned discrete quasi-static Hencky spring model (Sect. 1.3) a simple irreversible rupture mechanisms is considered for the springs. A spring is ruptured if its strain level exceeds (upper threshold) or is less than (lower threshold) a certain (constant) threshold. In particular, the criterion for rupture of a spring at iteration t, which discriminates whether that spring has to be removed from the computations at iteration $t+1$ or not, is based on (constant) thresholds for the relative elongation of extensional springs, e.g., $(\|p_{i+1,j} - p_{i,j}\| - \epsilon)$ (upper and lower thresholds are employed for this deformation measure). Upper thresholds for the relative rotation of adjacent springs belonging to the same fiber like, e.g., $(\cos\vartheta^1_{i,j} + 1)$ and for the relative rotation of adjacent springs belonging to different fibers like $|\vartheta^3_{i,j} - \frac{\pi}{2}|$ are contemplated but are not considered. Since the analyzed pantographic sheet is made out of a ductile material (polyamide), damage is governed by fiber breakage due to excessive extension rather than fiber breakage due to excessive bending or pivot failure due to torsion.

An experimental evidence [10] is provided by displacement-controlled uniaxial bias extension tests (Fig. 31) when performed on three different polyamide specimens. The first failure event was observed at the corners of the specimen, where the elongation of fibers is the highest.

This evidence is confirmed, through a different test [57] (see Fig. 32), since fiber elongation is the highest at the lower-left and upper-right corners. When the sample is made out of a brittle material, damage is governed by excessive shear strains (i.e., torsion of pivots) that, in the displacement-controlled uniaxial bias extension test, reaches its maximum near the two internal vertices of the quasi-rigidly deforming triangles.

In Ref. [57], a slow-rate (15 mm/min) of uniform horizontal displacement on the top of the specimen is prescribed. From the prescribed horizontal displacement $\overline{u}$, a non-dimensional displacement λ can be calculated. First fiber breakage is observed for a horizontal displacement $\overline{u} = 139.96$ mm (Fig. 32), which corresponds to a non-dimensional displacement $\lambda = 0.976$. By comparing Figs. 32 and 33, the model correctly predicts the location of fiber breakage. The "generalized" (because of the introduction of damage) numerical model fits well the force-displacement curve throughout the experiment, up to the onset of fiber breakage (Fig. 34).

In Ref. [58], pivot damage due to shear, i.e., fibers detaching due to friction in pivots, is taken into account, thereby allowing for sliding between the two families of fibers. Thus, the nonlinear homogenized quasi-static model for the discrete system in Fig. 11 (for more details about the homogenization procedure the reader is

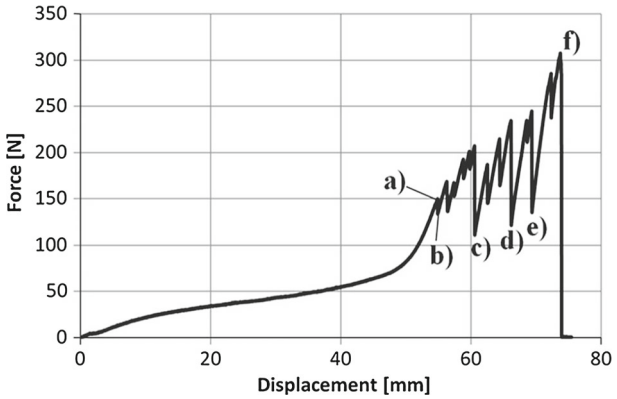

Fig. 31 Force versus prescribed displacement for a uniaxial bias extension test. **a** Sample before first beam breakage (i.e., breakdown onset); **b** upper-left corner beam breakage; **c**–**f** further fiber breakage

Fig. 32 **a** Reference configuration ($\lambda = 0$), **b** damage onset ($\lambda = 0.976$) of a shear test

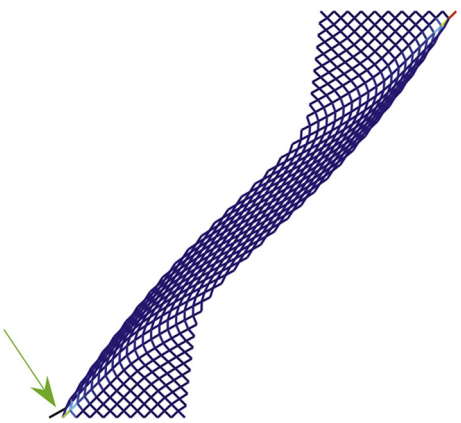

Fig. 33 Deformed configuration at the onset of damage. The broken fiber is colored in black, and it is pointed by the green arrow (color figure online)

referred to Ref. [13]) is modified by introducing, in the spirit of mixture theory, two independent placement functions χ^1 and χ^2 (the placement functions of body points belonging to horizontal and vertical fibers, respectively) defined on the same reference domain and, accordingly, considering the following nonlinear (elastic) strain energy to be minimized at each iteration

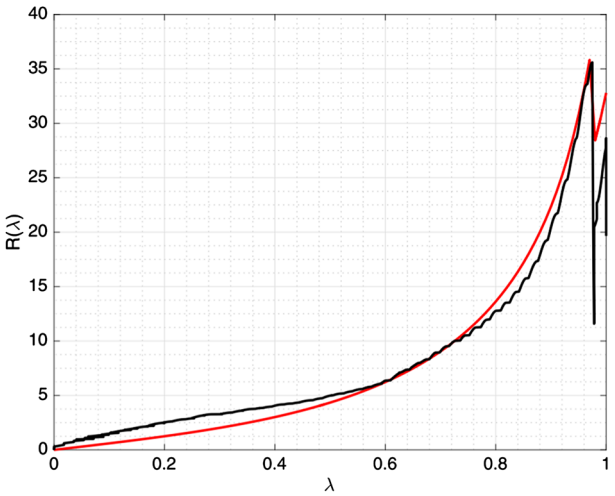

Fig. 34 Force (N) versus non-dimensional displacement for the shear test of a pantographic sheet up to the onset of fiber breakage. The black curve is the experimental data, and the red curve has been obtained via numerical simulation (color figure online)

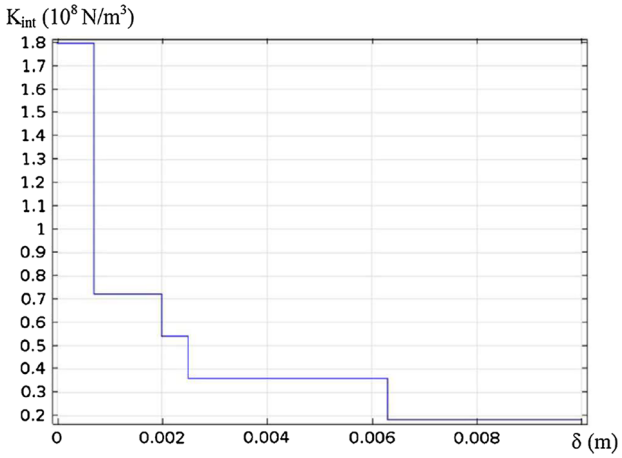

Fig. 35 Dependence of the resistance to sliding K_{int} on δ

$$\int_{\mathcal{B}_0} \underbrace{\sum_{\alpha=1,2} \frac{K_e^\alpha}{2} \|F^\alpha \hat{e}_\alpha - 1\|^2}_{\text{extension of horiz. and vert. fibers}} + \int_{\mathcal{B}_0} \underbrace{\frac{K_p}{2} \left| \arccos\left(\frac{F^1\hat{e}_1 \cdot F^2\hat{e}_2}{\|F^1\hat{e}_1\| \cdot \|F^2\hat{e}_2\|} \right) - \frac{\pi}{2} \right|^\xi}_{\text{shear (pivots torsion) contribution}} + \tag{44}$$

$$\int_{\mathcal{B}_0} \underbrace{\sum_{\alpha=1,2} \frac{K_b^\alpha}{2} \left[\frac{\|\nabla F^\alpha | \hat{e}_\alpha \otimes \hat{e}_\alpha\|^2}{\|F^\alpha \hat{e}_\alpha\|^2} - \left(\frac{F^\alpha \hat{e}_\alpha \cdot \nabla F^\alpha | \hat{e}_\alpha \otimes \hat{e}_\alpha}{\|F^\alpha \hat{e}_\alpha\|^2} \right)^2 \right]}_{\text{bending of horiz. and vert. fibers}} + \int_{\mathcal{B}_0} \underbrace{\frac{K_{\text{int}}}{2} \|\chi^1 - \chi^2\|^2}_{\text{relative sliding of the two layers}} \tag{45}$$

In Ref. [58], the relative sliding of two families of fibers is considered. A criterion based on thresholds for the relative distance $\delta = \|\chi^1 - \chi^2\|$ between χ^1 and χ^2 (e.g., the fitted K_{int} in Fig. 35) is presented.

A numerical example where an aluminum specimen is subject to uniaxial bias extension is shown. Constitutive parameters K_e^α, K_b^α, K_p and K_{int} were fitted using experimental data (Fig. 36), showing a very good agreement. The experiment is studied only up to the first rupture (i.e., as long as $K_{\text{int}} > 0 \; \forall X \in \mathcal{B}_0$). For the discrete model [57], and in turn for the continuum homogenized model [58] (as for their respective purely elastic counterparts), it is straightforward to implement the case of non-orthogonal initially straight fibers [60].

Further, the two models have been extensively tested when dealing with pure (nonlinear) elasticity, and they show a nearly perfect agreement with experimental results. In Fig. 37b, the onset of damage is observed at the

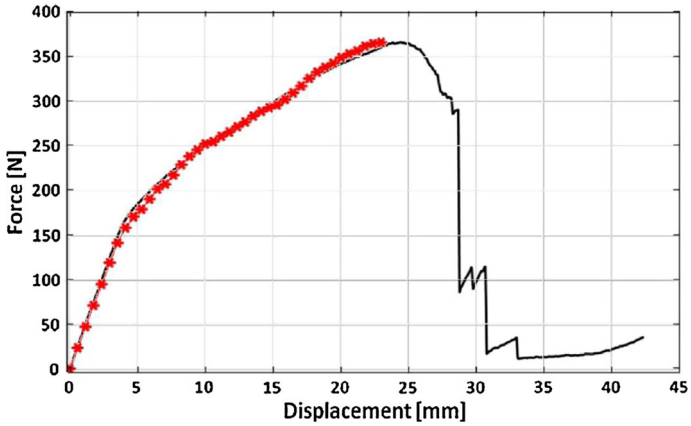

Fig. 36 Force versus applied displacement for a uniaxial bias extension test of an aluminum pantographic sheet. The black curve is the experimental measurement and the red obtained via numerical simulation (color figure online)

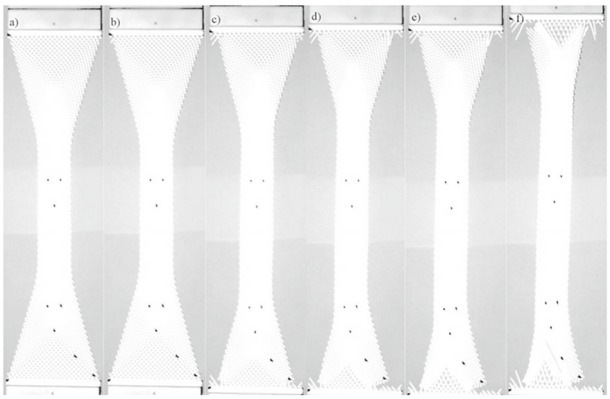

Fig. 37 A sample subject to uniaxial bias extension. **a** Sample before the first beam breakage (i.e., breakdown onset); **b** upper-left corner beam rupture; **c**–**f** rupture of further fibers

upper-left corner beam only. This is due to undesired asymmetries in the experimental setup (e.g., specimen, loading, clamping).

3 Feasibility of digital image correlation analyses

Up to now, the only reported kinematic data were prescribed macro-displacements or discrete measurements (e.g., control angles, see Fig. 17). In the future, it is desirable to have a richer experimental database in order to calibrate and validate in a more thorough way the previously discussed models. Since very large displacement levels occur, digital image correlation (DIC [61,62]) is a natural choice for the measurement technique. The feasibility of DIC on pantographic samples was shown very recently [63]. In that case study, a series of 30 load steps was analyzed with global DIC using meshes made of 3-noded triangles with linear shape functions (i.e., T3-DIC). Since the mesh was not compatible with the pantograph mesostructure, elastic regularization was used (i.e., so-called RT3-DIC [64]). In order to avoid any significant bias, the regularization length was identical to the element length (i.e., 25 pixels).

This example is further analyzed hereafter. Figure 38 shows the initial configuration, the last configuration prior to damage inception (i.e., 30th load step), and the broken sample. The grips were speckled for DIC purposes, and the hinges of the pantographic sheet were marked in black. A red background was used in order to create high contrast with the white color of pantographic sheet.

The first type of analysis consists in meshing the rectangular region of interest with T3 elements independently of the underlying mesostructure [63]. Such discretizations may then be compared with numerical simulations performed at the macroscale (as discussed above). Three different mesh densities are considered

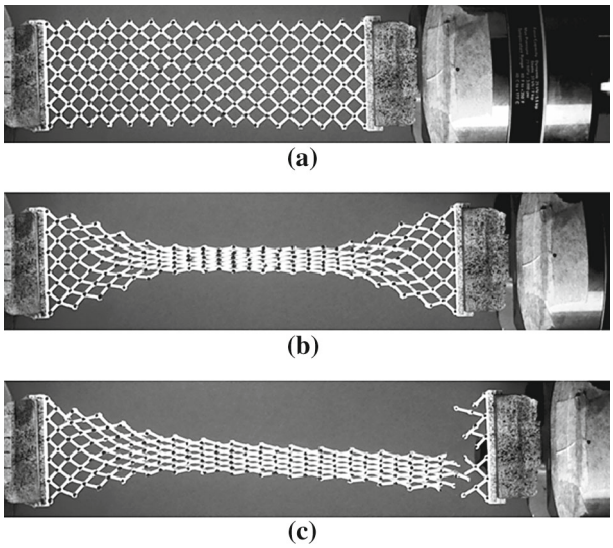

Fig. 38 Gray-level images of the pantograph in the reference configuration (**a**), last analyzed deformed configuration (**b**), and at failure (**c**)

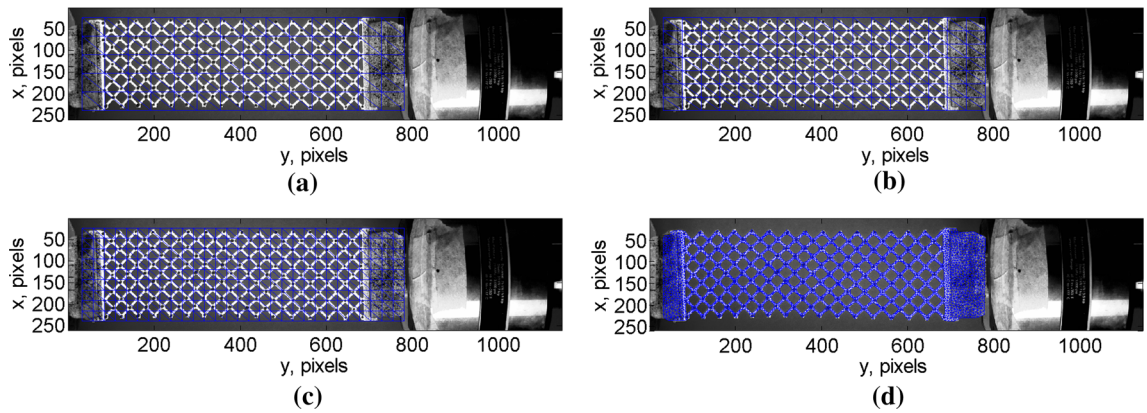

Fig. 39 Finite element meshes overlaid with the gray-level picture of the reference configuration

(Fig. 39a–c). The characteristic mesh size $\overline{\ell}$, which is defined as the square root of the average element surface, is equal to 34 pixels for the first mesh, 28 pixels for the second one, and 18 pixels for the third. Second, a fourth mesh was tailored to the pantograph surface (Fig. 39d). Thanks to the uniform background, simple morphological operations were performed in order to construct this mesoscale mesh from a mask. The characteristic mesh size is equal to 3.5 pixels.

Two types of registration routes are followed, namely the first one is an incremental approach that consists in updating the reference configuration that becomes the deformed configuration of the previous analysis. Its main advantage is that the elastic regularization only acts incrementally (i.e., equivalent to a hyperelastic description with Hencky strains). The convergence condition on the norm of the mean displacement correction was set to 10^{-3} pixel. The regularization length was selected to be equal to 45 pixels in that case. This choice enables the second, third and fourth meshes to be analyzed even though they are finer than the underlying mesostructure. The drawback is that measurement uncertainties are cumulated as more pictures are analyzed. A second option is to perform direct calculations that register the nth picture with that of the reference (i.e., unloaded) configuration. The measurement uncertainties are no longer cumulated. However, the elastic regularization may become too strong for the actual kinematics as it acts as a low-pass filter. Consequently, the regularization length was lowered to 30 pixels. The convergence condition on the norm of the mean displacement correction was set to 10^{-2} pixel since the measured displacement amplitudes will be significantly higher than in incremental registrations.

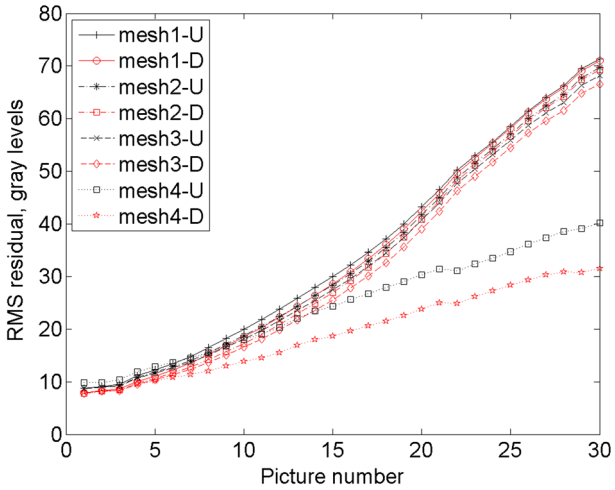

Fig. 40 RMS residual as a function of the picture number for the four meshes shown in Fig. 39. The extension U corresponds to updated registrations, and the extension D designates direct registrations

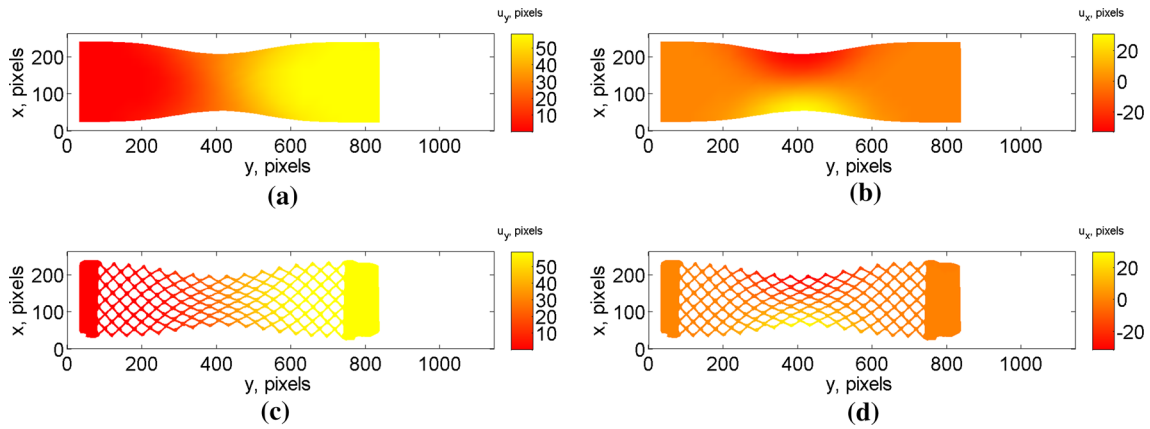

Fig. 41 Longitudinal (**a**–**c**) and transverse (**b**–**d**) displacement fields measured with meshes 3 (**a**, **b**) and 4 (**c**, **d**) for the 10th picture. The fields are shown on the deformed configuration

In T3-DIC, the quality of the registration is probed with the gray-level residual field, namely the pixelwise difference between the picture in the reference configuration and the picture in the deformed configuration corrected by the measured displacement field. The root-mean-square (RMS) average is reported in Fig. 40 for all eight situations considered herein. The first general trend is that the registration quality degrades as more steps are analyzed, thereby signaling that the measured fields do not fully capture the complex kinematics associated with the studied pantograph at the end of the experiment. Second, the direct registrations have always lower levels in comparison with updated registrations. This result validates the choice of the regularization strategy. Last, there is a clear difference between the first three meshes and the last one. This proves that a mesh tailored to the actual pantograph surface is able to better capture the kinematics of the test, even with the same regularization length as for the coarser meshes. In terms of measurement quality, the three meshes lead to similar overall residuals, which is to be expected because the regularization length is larger than the element size. For mesh 4, the gain between direct and updated registration is the highest.

In the following discussion, only two sets of results are reported, namely those of meshes 3 and 4 for direct registrations. Figure 41 shows the longitudinal and transverse displacements measured for the 10th picture. The transverse displacement field u_x shows that there is a huge contraction, which is of the order of magnitude as the longitudinal motions u_y. Given the fact that the width of the sample is one-third of its length, it proves that transverse deformations are much more important than the longitudinal component. This is due to the geometry of the pantographic sheet. The same observation applies for both meshes. In the present case, both measurements have approximately the same quality in terms of overall registration residuals (Fig. 40).

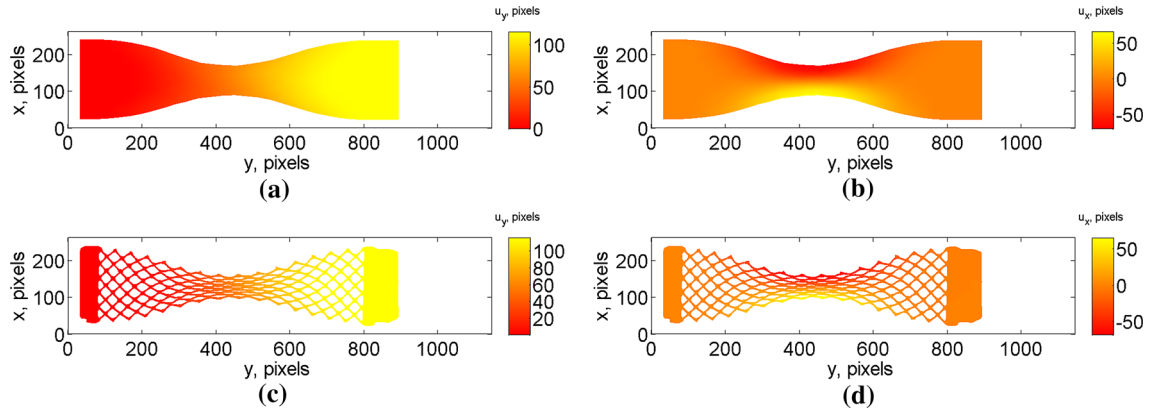

Fig. 42 Longitudinal (**a**–**c**) and transverse (**b**–**d**) displacement fields measured with meshes 3 (**a**, **b**) and 4 (**c**, **d**) for the 20th picture. The fields are shown on the deformed configuration

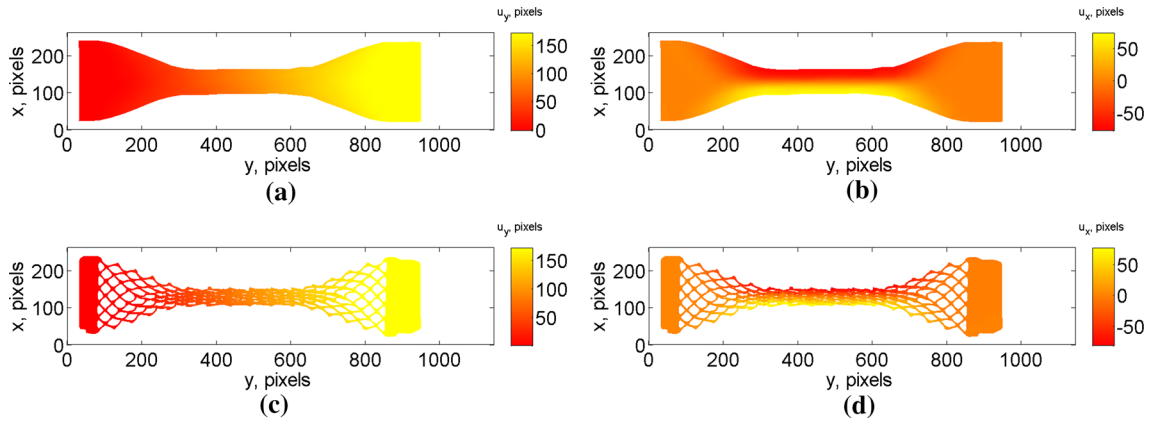

Fig. 43 Longitudinal (**a**–**c**) and transverse (**b**–**d**) displacement fields measured with meshes 3 (**a**, **b**) and 4 (**c**, **d**) for the 30th picture. The fields are shown on the deformed configuration

In Fig. 42, the same fields are shown for the 20th picture. The pattern of the transverse and longitudinal displacement fields is very similar with higher overall levels. The displacement ranges still are of the same order of magnitude for the longitudinal and transverse displacements. Consequently, the central part of the sample has become even thinner. The kinematic details are more easily observed for mesh 4. In this case, there is a clearer difference that translates into lower registration residuals for mesh 4 (Fig. 40).

The last load level prior to damage inception (i.e., first strut failure) is reported in Fig. 43. In that case, the gray-level residuals (Fig. 40) are significantly higher for mesh 3 in comparison with mesh 4. In both cases, the chosen kinematic basis is no longer able to completely describe the actual motions of the pantographic structure. For the parts of the pantographic sheet closer to the grips and the grips themselves, the registration quality is significantly better. This result validates the choice of including part of the speckled grips in the analysis. For this last step, the highly deformed region has grown toward both ends of the pantographic sheet, which can be understood by the fact that when struts touch each other, the deformation mechanism moves away from these zones.

The results reported herein show that DIC analyses can be run on pantographic structures at macroscopic *and* mesoscopic levels. Significant gains were observed in terms of registration quality by moving from the macroscopic to the mesoscopic scale (i.e., more than a factor of two at the end of the picture series). However, the final gray-level residuals indicate that even more refined approaches should be followed. What is missing in the mesoscopic analysis is the fact that pivots were not accounted for. This would require meshes to be constructed in such a way that the actual geometry of the pantographic structures would be described. Two options are possible. The first one would consist in using beam elements that are interconnected at the pivots. DIC analyses may then be easier since the number of degrees of freedom would be significantly reduced [65]. Second, instead of using beam elements, finite elements may also be considered with explicit descriptions

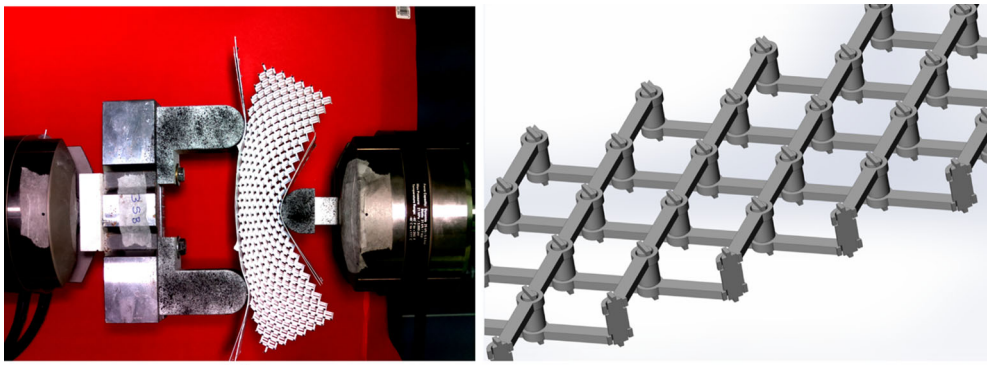

(a) **(b)**

Fig. 44 **a** Three-point flexural test on a 3D pantographic specimen. **b** Pantographic sheet with "perfect" hinges

of the pivots (as in the 3D Cauchy model, see Fig. 20). One challenge is to measure surface displacements with such very fine meshes since each element will contain very few pixels. This approach requires elastic regularizations to be considered [64] as performed herein. Last, integrated approaches may also be considered in which the displacement fields are derived thanks to numerical simulations and the material parameters then become the unknowns. In that case, the mesh can be as fine as wished since the number of unknowns has been drastically reduced [66,67].

4 Conclusion and outlook

Pantographic fabrics proved to be a very interesting subject of study, involving the work of, at least, (computational) mechanicians (modeling), experimentalists (experiments), numerical analysts (model solving), data analysts (image correlation), mathematicians (well-posedness and Γ-convergence) and many other researchers and professionals. We believe that what has been presented in this survey can thus be considered our manifesto about how commitment from different groups of researchers should be directed for the study of metamaterials and, more generally, for the study of every scientific subject. Mechanics, as any other natural science, cannot proceed without a continuous interplay between experimental evidence and theoretical modeling.

However, this is just a first simple step toward the study of more complex structures and experiments. A famous quote by Hilbert states that "the art of doing mathematics consists in finding that special case which contains all the germs of generality." This statement can be extended to every scientific discipline, including those that have been applied in the studies presented in this survey and that pantographic fabrics can be considered as one of the simplest examples leading to treat nonstandard problems in mechanics of materials and its related disciplines. In this sense, pantographic structures provide the minimal setting for the study of relevant issues in mechanics. The solution of a general problem is easier to face once that of its particular cases has been addressed, as, very often, particular cases help to understand better the real nature of the problem. Currently, new tests and structures are being studied, along with their technological realization challenges, like the three-point test shown in Fig. 44a and the pantographic sheet with "perfect" pivots, i.e., hinges that do not oppose to variations of the shear angle between two intersecting fibers, shown in Fig. 44b.

Acknowledgements This work was supported by a grant from the Government of the Russian Federation (contract No. 14.Y26.31.0031).

References

1. dell'Isola, F., Steigmann, D., Della Corte, A.: Synthesis of fibrous complex structures: designing microstructure to deliver targeted macroscale response. Appl. Mech. Rev. **67**(6), 060804 (2015)
2. Milton, G., Briane, M., Harutyunyan, D.: On the possible effective elasticity tensors of 2-dimensional and 3-dimensional printed materials. Math. Mech. Complex Syst. **5**(1), 41–94 (2017)
3. Eremeyev, V.A., Pietraszkiewicz, W.: Material symmetry group and constitutive equations of micropolar anisotropic elastic solids. Math. Mech. Solids **21**(2), 210–221 (2016)
4. Bertram, A., Glüge, R.: Gradient materials with internal constraints. Math. Mech. Complex Syst. **4**(1), 1–15 (2016)

5. Russo, L.: The Forgotten Revolution: How Science Was Born in 300 BC and Why It Had to Be Reborn. Springer, Berlin (2013)
6. Stigler, S.M.: Stigler's law of eponymy. Trans. N. Y. Acad. Sci. **39**(1 Series II), 147–157 (1980)
7. dell'Isola, F., Andreaus, U., Placidi, L.: At the origins and in the vanguard of peridynamics, non-local and higher-gradient continuum mechanics: an underestimated and still topical contribution of Gabrio Piola. Math. Mech. Solids **20**(8), 887–928 (2015)
8. dell'Isola, F., Corte, A.D., Giorgio, I.: Higher-gradient continua: the legacy of Piola, Mindlin, Sedov and Toupin and some future research perspectives. Math. Mech. Solids **22**(4), 852–872 (2017)
9. Del Vescovo, D., Giorgio, I.: Dynamic problems for metamaterials: review of existing models and ideas for further research. Int. J. Eng. Sci. **80**, 153–172 (2014)
10. dell'Isola, F., Lekszycki, T., Pawlikowski, M., Grygoruk, R., Greco, L.: Designing a light fabric metamaterial being highly macroscopically tough under directional extension: first experimental evidence. Z. angew. Math. Phys. **66**, 3473–3498 (2015)
11. Alibert, J.-J., Seppecher, P., dell'Isola, F.: Truss modular beams with deformation energy depending on higher displacement gradients. Math. Mech. Solids **8**(1), 51–73 (2003)
12. Pideri, C., Seppecher, P.: A second gradient material resulting from the homogenization of an heterogeneous linear elastic medium. Contin. Mech. Thermodyn. **9**(5), 241–257 (1997)
13. dell'Isola, F., Giorgio, I., Pawlikowski, M., Rizzi, N.: Large deformations of planar extensible beams and pantographic lattices: heuristic homogenization, experimental and numerical examples of equilibrium. Proc. R. Soc. A **472**(2185), 23 (2016)
14. dell Isola, F., Seppecher, P., Della Corte, A.: The postulations á la d alembert and á la cauchy for higher gradient continuum theories are equivalent: a review of existing results. In: Proceedings of the Royal Society A, Volume 471, p. 20150415. The Royal Society (2015)
15. Auffray, N., dell'Isola, F., Eremeyev, V., Madeo, A., Rosi, G.: Analytical continuum mechanics à la Hamilton–Piola least action principle for second gradient continua and capillary fluids. Math. Mech. Solids **20**(4), 375–417 (2015)
16. Altenbach, H., Eremeyev, V.: On the linear theory of micropolar plates. ZAMM **89**(4), 242–256 (2009)
17. Pietraszkiewicz, W., Eremeyev, V.: On natural strain measures of the non-linear micropolar continuum. Int. J. Solids Struct. **46**(3), 774–787 (2009)
18. Rahali, Y., Giorgio, I., Ganghoffer, J.F., dell'Isola, F.: Homogenization à la piola produces second gradient continuum models for linear pantographic lattices. Int. J. Eng. Sci. **97**, 148–172 (2015)
19. Bilotta, A., Formica, G., Turco, E.: Performance of a high-continuity finite element in three-dimensional elasticity. Int. J. Numer. Methods Biomed. Eng. **26**(9), 1155–1175 (2010)
20. Cazzani, A., Malagù, M., Turco, E.: Isogeometric analysis: a powerful numerical tool for the elastic analysis of historical masonry arches. Contin. Mech. Thermodyn. **28**(1–2), 139–156 (2016)
21. de Saint-Venant, M.: Mémoire sur la torsion des prismes: avec des considérations sur leur flexion ainsi que sur l'équilibre intérieur des solides élastiques en général: et des formules pratiques pour le calcul de leur résistance à divers efforts s' exerçant simultanément. Imprimerie nationale (1856)
22. Mindlin, R.D., Tiersten, H.F.: Effects of couple-stresses in linear elasticity. Arch. Ration. Mech. Anal. **11**(1), 415–448 (1962)
23. Dillon, O.W., Perzyna, P.: Gradient theory of materials with memory and internal changes. Arch. Mech. **24**(5–6), 727–747 (1972)
24. Abdoul-Anziz, H., Seppecher, P.: Strain gradient and generalized continua obtained by homogenizing frame lattices (2017) . <hal-01672898>
25. Turco, E., Giorgio, I., Misra, A., dell'Isola, F.: King post truss as a motif for internal structure of (meta) material with controlled elastic properties. Open Sci. **4**(10), 171153 (2017)
26. Everstine, G.C., Pipkin, A.C.: Boundary layers in fiber-reinforced materials. J. Appl. Mech. **40**, 518–522 (1973)
27. Hilgers, M.G., Pipkin, A.C.: Elastic sheets with bending stiffness. Q. J. Mech. Appl. Math. **45**, 57–75 (1992)
28. Hilgers, M.G., Pipkin, A.C.: Energy-minimizing deformations of elastic sheets with bending stiffness. J. Elast. **31**, 125–139 (1993)
29. Hilgers, M.G., Pipkin, A.C.: Bending energy of highly elastic membranes ii. Q. Appl. Math. **54**, 307–316 (1996)
30. Hu, M.Z., Kolsky, H., Pipkin, A.C.: Bending theory for fiber-reinforced beams. J. Compos. Mater. **19**, 235–249 (1985)
31. Pipkin, A.C.: Generalized plane deformations of ideal fiber-reinforced materials. Q. Appl. Math. **32**, 253–263 (1974)
32. Pipkin, A.C.: Energy changes in ideal fiber-reinforced composites. Q. Appl. Math. **35**, 455–463 (1978)
33. Pipkin, A.C.: Some developments in the theory of inextensible networks. Q. Appl. Math. **38**, 343–355 (1980)
34. dell'Isola, F., d'Agostino, M.V., Madeo, A., Boisse, P., Steigmann, D.: Minimization of shear energy in two dimensional continua with two orthogonal families of inextensible fibers: the case of standard bias extension test. J. Elast. **122**(2), 131–155 (2016)
35. Placidi, L., Greco, L., Bucci, S., Turco, E., Rizzi, N.L.: A second gradient formulation for a 2d fabric sheet with inextensible fibres. Z. angew. Math. Phys. **67**(5), 114 (2016)
36. Rivlin, R.S.: Plane strain of a net formed by inextensible cords. In: Collected Papers of RS Rivlin, pp. 511–534. Springer (1997)
37. Greco, L., Giorgio, I., Battista, A.: In plane shear and bending for first gradient inextesible pantographic sheets: numerical study of deformed shapes and global constraint reactions. Math. Mech. Solids, p. 1081286516651324 (2016)
38. Cuomo, M., Dell'Isola, F., Greco, L., Rizzi, N.L.: First versus second gradient energies for planar sheets with two families of inextensible fibres: investigation on deformation boundary layers, discontinuities and geometrical instabilities. Compos. B Eng. **115**, 423–448 (2017)
39. Cuomo, M., dell'Isola, F., Greco, L.: Simplified analysis of a generalized bias test for fabrics with two families of inextensible fibres. Z. angew. Math. Phys. **67**(3), 1–23 (2016)
40. dell'Isola, F., Cuomo, M., Greco, L., Della Corte, A.: Bias extension test for pantographic sheets: numerical simulations based on second gradient shear energies. J. Eng. Math. **103**(1), 127–157 (2017)

41. Greco, L., Giorgio, I., Battista, A.: In plane shear and bending for first gradient inextensible pantographic sheets: numerical study of deformed shapes and global constraint reactions. Math. Mech. Solids **22**(10), 1950–1975 (2017)
42. Giorgio, I.: Numerical identification procedure between a micro-cauchy model and a macro-second gradient model for planar pantographic structures. Z. angew. Math. Phys. **67**(4), 95 (2016)
43. Turco, E., dell'Isola, F., Cazzani, A., Rizzi, N.L.: Hencky-type discrete model for pantographic structures: numerical comparison with second gradient continuum models. Z. angew. Math. Phys. **67**, 28 (2016)
44. Eremeyev, V.A., dell'Isola, F., Boutin, C., Steigmann, D.: Linear pantographic sheets: existence and uniqueness of weak solutions (2017). https://doi.org/10.1007/s10659-017-9660-3
45. Placidi, L., Barchiesi, E., Turco, E., Rizzi, N.L.: A review on 2D models for the description of pantographic fabrics. Z. angew. Math. Phys. **67**(5), 121 (2016)
46. dell'Isola, F., Steigmann, D.J.: A two-dimensional gradient-elasticity theory for woven fabrics. J. Elast. **18**, 113–125 (2015)
47. Giorgio, I., Grygoruk, R., dell'Isola, F., Steigmann, D.J.: Pattern formation in the three-dimensional deformations of fibered sheets. Mech. Res. Commun. **69**, 164–171 (2015)
48. Giorgio, I., Rizzi, N.L., Turco, E.: Continuum modelling of pantographic sheets for out-of-plane bifurcation and vibrational analysis. Proc. R. Soc. A, p. 21 (2017). https://doi.org/10.1098/rspa.2017.0636
49. Auffray, N., Dirrenberger, J., Rosi, G.: A complete description of bi-dimensional anisotropic strain-gradient elasticity. Int. J. Solids Struct. **69**, 195–206 (2015)
50. Boutin, C., dell'Isola, F., Giorgio, I., Placidi, L.: Linear pantographic sheets: asymptotic micro–macro models identification. Math. Mech. Complex Syst. **5**(2), 127–162 (2017)
51. Placidi, L., Andreaus, U., Corte, A.D., Lekszycki, T.: Gedanken experiments for the determination of two-dimensional linear second gradient elasticity coefficients. Z. angew. Math. Phys. **66**(6), 3699–3725 (2015)
52. Placidi, L., Barchiesi, E., Battista, A.: An inverse method to get further analytical solutions for a class of metamaterials aimed to validate numerical integrations. In: Mathematical Modelling in Solid Mechanics, pp. 193–210. Springer (2017)
53. Scerrato, D., Zhurba Eremeeva, I.A., Lekszycki, T., Rizzi, N.L., Rizzi, N.L.: On the effect of shear stiffness on the plane deformation of linear second gradient pantographic sheets. ZAMM **96**(11), 1268–1279 (2016)
54. dell'Isola, F., Giorgio, I., Andreaus, U.: Elastic pantographic 2d lattices: a numerical analysis on static response and wave propagation. Proc. Est. Acad. Sci. **64**, 219–225 (2015)
55. dell'Isola, F., Della Corte, A., Giorgio, I., Scerrato, D.: Pantographic 2D sheets. Int. J. Non Linear Mech. **80**, 200–208 (2016)
56. Madeo, A., Della Corte, A., Greco, L., Neff, P.: Wave propagation in pantographic 2d lattices with internal discontinuities. arXiv preprint arXiv:1412.3926 (2014)
57. Turco, E., dell'Isola, F., Rizzi, N.L., Grygoruk, R., Müller, W.H., Liebold, C.: Fiber rupture in sheared planar pantographic sheets: numerical and experimental evidence. Mech. Res. Commun. **76**, 86–90 (2016)
58. Spagnuolo, M., Barcz, K., Pfaff, A., Dell'Isola, F., Franciosi, P.: Qualitative pivot damage analysis in aluminum printed pantographic sheets: numerics and experiments. Mech. Res. Commun. **83**, 47–52 (2017)
59. Ganzosch, G., dell'Isola, F., Turco, E., Lekszycki, T., Müller, W.H.: Shearing tests applied to pantographic structures. Acta Polytech. CTU Proc. **7**, 1–6 (2016)
60. Turco, E., Golaszewski, M., Giorgio, I., D'Annibale, F.: Pantographic lattices with non-orthogonal fibres: experiments and their numerical simulations. Compos. B Eng. **118**, 1–14 (2017)
61. Sutton, M.A., Orteu, J.J., Schreier, H.: Image Correlation for Shape, Motion and Deformation Measurements: Basic Concepts, Theory and Applications. Springer, Berlin (2009)
62. Hild, F., Roux, S.: Digital Image Correlation, pp. 183–228. Wiley-VCH, Weinheim (2012)
63. Turco, E., Misra, A., Pawlikowski, M., dell'Isola, F., Hild, F.: Enhanced piola-hencky discrete models for pantographic sheets with pivots without deformation energy: numerics and experiments (submitted for publication) (2018)
64. Tomičević, Z., Hild, F., Roux, S.: Mechanics-aided digital image correlation. J. Strain Anal. Eng. Des. **48**(5), 330–343 (2013)
65. Hild, F., Roux, S., Gras, R., Guerrero, N., Marante, M.E., Flórez-López, J.: Displacement measurement technique for beam kinematics. Opt. Lasers Eng. **47**(3), 495–503 (2009)
66. Leclerc, H., Périé, J.-N., Roux, S., Hild, F.: Integrated digital image correlation for the identification of mechanical properties. In: Gagalowicz, A., Philips, W. (eds.) International Conference on Computer Vision/Computer Graphics Collaboration Techniques and Applications, Volume LNCS 5496, pp. 161–171. Springer, Berlin (2009)
67. Lindner, D., Mathieu, F., Hild, F., Allix, O., Ha Minh, C., Paulien-Camy, O.: On the evaluation of stress triaxiality fields in a notched titanium alloy sample via integrated DIC. J. Appl. Mech. **82**(7), 071014 (2015)